RESEARCH ARTICLE

Key Points:
- Development of OMI SO_2 vertical column algorithm
- Results are compared to ground-based and satellite data sets
- The algorithm is able to detect weak SO_2 sources

Correspondence to:
N. Theys,
theys@aeronomie.be

Sulfur dioxide vertical column DOAS retrievals from the Ozone Monitoring Instrument: Global observations and comparison to ground-based and satellite data

N. Theys[1], I. De Smedt[1], J. van Gent[1], T. Danckaert[1], T. Wang[1,2], F. Hendrick[1], T. Stavrakou[1], S. Bauduin[3], L. Clarisse[3], C. Li[4,5], N. Krotkov[5], H. Yu[1], H. Brenot[1], and M. Van Roozendael[1]

[1]Belgian Institute for Space Aeronomy, Brussels, Belgium, [2]Institute of Atmospheric Physics, Chinese Academy of Sciences, Beijing, China, [3]Spectroscopie de l'Atmosphère, Service de Chimie Quantique et Photophysique, Université Libre de Bruxelles, Brussels, Belgium, [4]Earth System Science Interdisciplinary Center, University of Maryland, College Park, Maryland, USA, [5]NASA Goddard Space Flight Center, Greenbelt, Maryland, USA

Abstract We present a new data set of sulfur dioxide (SO_2) vertical columns from observations of the Ozone Monitoring Instrument (OMI)/AURA instrument between 2004 and 2013. The retrieval algorithm used is an advanced Differential Optical Absorption Spectroscopy (DOAS) scheme combined with radiative transfer calculation. It is developed in preparation for the operational processing of SO_2 data product for the upcoming TROPOspheric Monitoring Instrument/Sentinel 5 Precursor mission. We evaluate the SO_2 column results with those inferred from other satellite retrievals such as Infrared Atmospheric Sounding Interferometer and OMI (Linear Fit and Principal Component Analysis algorithms). A general good agreement between the different data sets is found for both volcanic and anthropogenic SO_2 emission scenarios. We show that our algorithm produces SO_2 columns with low noise and is able to provide accurate estimates of SO_2. This conclusion is supported by important validation results over the heavily polluted site of Xianghe (China). Nearly 4 years of OMI and ground-based multiaxis DOAS SO_2 columns are compared, and an excellent match is found. We also highlight the improved performance of the algorithm in capturing weak SO_2 sources by detecting shipping SO_2 emissions in long-term averaged data, an unreported measurement from space.

1. Introduction

Sulfur dioxide (SO_2) is emitted to the atmosphere from anthropogenic and natural sources. Anthropogenic emissions are mostly from combustion of fossil fuels (coal and oil) and metal smelting. The main natural source of nonvolcanic sulfur in the boundary layer is the oxidation of biogenic dimethyl sulfide from the oceans, but in the upper troposphere and lower stratosphere (UTLS), volcanic eruptions constitute the largest natural contributor of SO_2. Sulfur dioxide is depleted in the atmosphere either through deposition or oxidation mechanisms, the latter leading to aerosol formation. The reactive compounds can have adverse effects on surrounding environments (acid rain), air quality [*Chin and Jacob*, 1996], weather, clouds, and climate [*Intergovernmental Panel on Climate Change*, 2013]. In the stratosphere, the forcing from sulfate aerosols can have a transient impact on global climate for several years after strong volcanic eruptions [*Robock*, 2000].

Satellite observations of SO_2 are a key data source for assessing global SO_2 budget and chemistry, studying air pollution, and monitoring volcanic activity and related hazardous clouds. In particular, nadir ultraviolet (UV) sounding is well suited to detect SO_2 from both volcanic and anthropogenic sources, owing to good sensitivity to SO_2 in the lower troposphere. SO_2 has strong absorption bands in the UV spectral range, and the total SO_2 vertical column density (VCD, hereafter expressed in Dobson Unit—1 DU = 2.69×10^{16} molecules cm^{-2}) can be retrieved from satellite measurements of solar backscattered UV radiation, albeit with significant uncertainty. Satellite UV remote sensing of SO_2 VCD has been achieved by the following instruments: Total Ozone Mapping Spectrometer [*Krueger et al.*, 1995; *Carn et al.*, 2004], Global Ozone Monitoring Experiment (GOME-2) [*Eisinger and Burrows*, 1998; *Khokhar et al.*, 2005], Scanning Imaging Absorption Spectrometer for Atmospheric Chartography (SCIAMACHY) [*Richter et al.*, 2006; *Lee et al.*, 2009], GOME-2 [*Richter et al.*, 2009a;

Nowlan et al., 2011; *Rix et al.*, 2012], Ozone Monitoring Instrument (OMI) [*Krotkov et al.*, 2006; *Yang et al.*, 2007], and Ozone Mapping and Profiler Suite (OMPS) [*Yang et al.*, 2013]. The OMI UV mapper is particularly appealing as it combines hyperspectral measurement capability at high signal-to-noise ratio with high spatial resolution (pixel size is $13 \times 24\,km^2$ at nadir) and daily global coverage [*Levelt et al.*, 2006]. Sulfur dioxide retrievals from OMI have been used quite extensively to measure volcanic degassing (a review is provided by *Carn et al.* [2013]) and anthropogenic emissions [e.g., *Carn et al.*, 2007; *Krotkov et al.*, 2008; *Li et al.*, 2010; *Fioletov et al.*, 2011; *Lu et al.*, 2013]. Recently, *Fioletov et al.* [2013] showed that long-term averaged SO_2 retrievals by OMI, GOME-2, and SCIAMACHY were generally in good quantitative agreement over large emission sources, when using consistent assumptions for the radiative transfer and after applying local bias filtration techniques. They also demonstrated the improved detection of small sources by OMI compared to the other sensors.

In this paper, we present a new OMI algorithm to determine SO_2 columns by applying a multiwindows Differential Optical Absorption Spectroscopy (DOAS) scheme [*Platt and Stutz*, 2008], which results in robust retrievals with low noise. The presented retrieval scheme will form the basis of the algorithm for the operational level 2 SO_2 data product from the forthcoming TROPOspheric Monitoring Instrument (TROPOMI) instrument on board the Sentinel-5 Precursor mission [*Veefkind et al.*, 2012]. With improved signal-to-noise level and spatial resolution (pixel size ~ $7 \times 7\,km^2$) compared to OMI, the TROPOMI sensor will have enhanced capabilities for global SO_2 measurements. The motivation of this study is to demonstrate the performance of the TROPOMI algorithm using OMI measured spectra for several examples of volcanic and anthropogenic SO_2 emissions. We evaluate our SO_2 product through comparisons with other satellite retrievals in the thermal infrared (Infrared Atmospheric Sounding Interferometer, IASI) and ultraviolet. In particular, the new SO_2 columns are compared to those from the standard OMI SO_2 products. Presently, two algorithms are employed for the OMI standard products.

1. The Linear Fit (LF) OMI SO_2 retrieval algorithm [*Yang et al.*, 2007]. This algorithm is used to produce retrievals of SO_2 total columns for a set of hypothetical SO_2 profiles with SO_2 distributed in the lower troposphere, the midtroposphere, and the lower stratosphere (STL), corresponding to SO_2 plumes from volcanic degassing, modest eruption, and strong eruption, respectively. It exploits the residuals from OMI total column O_3 retrievals at 10 discrete wavelengths between 310.8 and 360.15 nm. Shorter wavelengths are dropped in the retrievals for large volcanic plumes, in order to reduce negative biases due to saturation of SO_2 absorption. A sliding median residual correction technique is applied in the LF algorithm to reduce retrieval biases.
2. The new principal component analysis (PCA) OMI SO_2 retrieval algorithm [*Li et al.*, 2013]. This algorithm applies the PCA technique to OMI-measured radiances between 310.5 and 340 nm to extract principal components (PCs) from each row on an orbital basis. The leading PCs that capture a large fraction of the spectral variance are associated with various processes that interfere with SO_2 signals, including O_3 absorption, the Ring effect, etc. These PCs are fitted along with precomputed SO_2 Jacobians to produce estimates of the SO_2 total column. No bias correction is currently applied in the PCA algorithm. It has replaced the Band Residual Difference algorithm [*Krotkov et al.*, 2006] as the operational algorithm for the standard OMI planetary boundary layer (PBL) SO_2 data (assuming SO_2 mostly in the PBL). Compared with the previous OMI PBL SO_2 product, the PCA product shows large reduction in both systematic bias and retrieval noise. As shown below, the DOAS and PCA algorithms are in good agreement and have comparable performances, giving confidence to both approaches.

Another important part of the present study is the validation of the retrievals against ground-based multiaxis (MAX-)DOAS measurements at Xianghe (suburban Beijing, China). The long-term MAX-DOAS SO_2 measurements improve upon previous validation studies based on in situ measurements [*Krotkov et al.*, 2008; *Lee et al.*, 2009; *He et al.*, 2012] that suffer from spatial-temporal sampling and/or extrapolation issues. Finally, the improvements in SO_2 data are demonstrated using long-term averages that show evidence for SO_2 pollution from shipping that has not been observed from space before.

In section 2 we give an overview of OMI and the algorithm to retrieve SO_2 vertical columns. Examples of results and comparison to ground-based and satellite data are presented for cases with SO_2 from volcanic (section 3.1) and anthropogenic sources (section 3.2). Conclusions are given in section 4.

2. Algorithm Description

The Ozone Monitoring Instrument (OMI) is a nadir-viewing instrument on the EOS-Aura satellite of NASA (launched in July 2004) flying in a Sun-synchronous polar orbit with an equator crossing time of about 13:38 local time in the ascending node. OMI is an imaging spectrograph that measures reflected-backscattered sunlight in the ultraviolet-visible range from 270 nm to 500 nm with a spectral resolution of about 0.5 nm [*Levelt et al.*, 2006]. OMI is a CCD (charge-coupled device) push-broom instrument, recording the complete spectrum in along-track direction, and sensing the atmosphere with a 114° field of view, separated in 60 discrete viewing angles, perpendicular to the flight direction (across track). The OMI spatial swath is 2600 km wide allowing complete global coverage in about 1 day. The OMI ground pixel size varies from 13×24 km^2 at nadir to 28×150 km^2 at the edges of the swath. Since June 2007, the radiance data of OMI are altered at all wavelengths for some particular viewing directions corresponding to specific rows of the 2-D CCD. This so-called row anomaly (see http://www.knmi.nl/omi/research/product/rowanomaly-background.php) is due to a partial blockage affecting the nadir-viewing port of the sensor. It changes with time and position on the orbit; from 2008 onward, it affects seriously the quality of some measured spectra and hence reduces the spatial coverage (section 2.2).

The algorithm to retrieve SO$_2$ vertical columns from OMI measurements is based on three main steps, described in the next sections, that include analysis of the measured spectra, background correction scheme, and radiative transfer simulations.

2.1. DOAS Retrieval

OMI radiance measurements from Level 1 data version 2.13 are analyzed using the DOAS method for the determination of the columnar concentration of SO$_2$ along the effective light path through the atmosphere (hereafter referred as slant column density, SCD). Briefly, absorption cross sections of relevant atmospheric gases are adjusted by a nonlinear least squares fit procedure to the log ratio of a measured earthshine spectrum and a reference spectrum in a given wavelength interval. The DOAS fit also includes additional closure terms for the Ring effect and contributions from broadband and instrumental spectral features.

In practice, SO$_2$ slant columns have been retrieved with QDOAS [*Fayt and Van Roozendael*, 2001; *Danckaert et al.*, 2012], a versatile software for trace gas retrievals in the UV-visible spectral range, which has been adapted for OMI spectra. In particular, each row of OMI is treated in the analysis as a separate detector (hence characterized by a proper wavelength-dependent slit function). This also holds true for the wavelength calibration step.

The DOAS analysis settings used to retrieve SO$_2$ SCDs are detailed in Table 1. As a baseline, SO$_2$ is retrieved in the sensitive 312–326 nm window (labeled w1 in the following), which includes strong SO$_2$ absorption bands (Figure 1). In this interval, the absorption is dominated by total ozone, and two ozone cross sections at 228 K and 243 K are included in the fit. Furthermore, two additional pseudo cross sections are introduced in the analysis to better cope with nonlinear effects due to ozone absorption. Following the formulation of *Puķīte et al.* [2010], these spectra correspond to the two terms of the first-order Taylor expansion of the ozone optical depth. This approach allows us to improve the results at high solar zenith angle (SZA; $\gtrsim45°$) by reducing the fitting residuals (up to a factor of two) and the bias on the SO$_2$ slant columns (see next section). We have estimated the noise level on the retrieved SO$_2$ SCDs by the SCD data scatter (1σ value) around the mean for solar zenith angle (SZA) bins and by excluding polluted regions and strong volcanic eruptions. It is typically 0.2–0.5 DU depending on the solar zenith angle. Tests using the 315–326 nm fitting interval [*Richter et al.*, 2006; *Rix et al.*, 2012] increase the data scatter by a factor of 2, as expected by the noninclusion in the fit of the strong SO$_2$ band peaking at around 313 nm. We have done further tests by extending the fitting window to 310.5–326 nm (including one more SO$_2$ band), but these show only a small improvement as for the data scatter, probably because of the competing strong ozone absorption in the short UV (Figure 1) causing a drop in intensity (and in signal-to-noise ratio). Therefore, we have not selected the fitting window 310.5–326 nm as the sensitivity to SO$_2$ absorption in the lower troposphere is somewhat lower than for the 312–326 nm range (mostly because of increasing ozone absorption below 312 nm).

Whereas SO$_2$ retrieval in w1 is adequate for small SO$_2$ column amount, it has limited accuracy once the SO$_2$ signal is large (for scenes with high SO$_2$ amounts from volcanic eruptions), typically leading to a saturation of

Table 1. DOAS Settings Used to Retrieve SO$_2$ Columns From OMI Spectra[a]

Fitting Intervals 1 and 2 (UV-2 Channel:307–383 nm)	312–326 nm (w1), 325–335 nm (w2)
Cross sections	SO$_2$ 203 K; *Bogumil et al.* [2003]
	O$_3$ 228 K and 243 K with I$_0$ correction; *Brion et al.* [1998]
	Pseudo O$_3$ cross sections ($\lambda\sigma_{O3}$, σ_{O3}^2); *Puķīte et al.* [2010]
	Ring effect: 2 eigenvectors (*Vountas et al.* [1998]) generated for 20° and 87° solar zenith angles using LIDORT-RRS; *Spurr* [2008]
Polynomial	Fifth Order
Fitting interval 3 (VIS channel:349–504 nm)	360–390 nm (w3)
Cross sections	SO$_2$ *Hermans et al.* [2009] extrapolated at 203 K
	NO$_2$ 220 K; *Vandaele et al.* [1998]
	O$_2$–O$_2$; *Greenblatt et al.* [1990]
	Ring effect: single spectrum; *Chance and Spurr* [1997]
Polynomial	Fourth order
Intensity offset correction	Linear offset
Spectrum shift and stretch	Fitted
Spectral spikes removal procedure	*Richter et al.* [2011]
Reference spectrum	Daily averaged earthshine spectrum in Pacific region (10°S–10°N, 160°E–120°W); separate spectrum for each detector row
Fitting interval selection criteria	w1: baseline
	w2: SCD1 > 40 DU or SCD1 > 15 DU if fit residual w1 > 10^{-2} SCD2 > SCD1
	w3: SCD2 > 250 DU and SCD3 > SCD2

[a]The cross sections are convolved with the instrumental wavelength-dependent slit functions [*Dobber et al.*, 2006] separately for each of the 60 detector rows.

the retrieved SO$_2$ SCD due to nonlinear retrieval effects from strong absorption by SO$_2$ itself [e.g., *Richter et al.*, 2009; *Yang et al.*, 2007]. To overcome this problem, alternative fitting windows (w2 and w3) are considered: 325–335 nm [*Hörmann et al.*, 2013] and 360–390 nm for extreme SO$_2$ loadings [*Bobrowski et al.*, 2010]. We have conducted several sensitivity tests, based on synthetic and measured spectra, to assess the best use of the different fitting intervals. SCDi have been retrieved for all wi ($i = 1, 2, 3$), and the applicability of the three fitting windows was determined empirically by means of scatterplots (see e.g., Figure S1 in the supporting information). The combined use of the three data sets is achieved according to the criteria given in Table 1. Note that SO$_2$ cross sections are used for a fixed temperature of 203 K, which is valid for a volcanic SO$_2$ plume in the tropical UTLS. For lower plumes and anthropogenic pollution, the retrievals in w1 tend to underestimate the SO$_2$ SCDs by up to 15%.
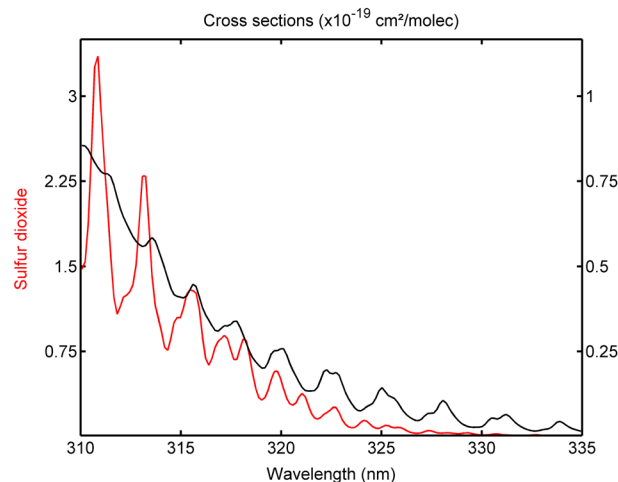

Figure 1. Absorption cross sections of SO$_2$ (203 K) and O$_3$ (228 K) at the spectral resolution of OMI between 310 and 335 nm.

2.2. Treatment of the Row Anomaly and Background Correction

The next step of the algorithm deals with filtering of the pixels affected by the row anomaly. The row anomaly flag included in the OMI operational L1B product has the tendency to classify more pixels as affected than strictly necessary; therefore, we have set up a new identification of row anomaly-affected pixels. We first apply a criterion that removes all data of a given day for certain across-track positions. The selection is based on w1 fitting residuals over a latitude band around the equator (10°S–10°N), which show typically anomalous high values for the affected rows. A given row is

classified as affected by the row anomaly if the mean residual over the equator is larger than the corresponding residual averaged for all rows, by more than 20%. To avoid contamination by a possible strong volcanic SO_2 signal or an artifact (e.g. due to the South Atlantic Anomaly), we only consider the pixels with slant columns less than 5 DU and residuals lower than 4×10^{-3} for the calculation of the averages. After this first selection, we apply a second criterion to filter data affected by the row anomaly. It is a simple selection based on the fitting residuals and is meant for an anomaly corrupting only a part of the orbit: pixels with fitting residuals larger than 4×10^{-3}, but SCDs lower than 5 DU are rejected. The condition on the SCD is used to keep the pixels with real elevated SO_2 (and hence high-fitting residuals). The above-described filtering of the row anomaly proved to be a good compromise between the number of retained observations and the data quality.

After the data filtering step, a background correction is applied to the resulting SCDs. This is particularly important for retrievals in the baseline window. SCDs typically show unphysical nonzero columns over certain clean regions (e.g. the tropical pacific, deserts, and high-altitude regions). While the reason for this behavior is not completely clear, the observed bias is time dependent and is more pronounced for strong ozone absorption (at high latitudes). The correction we use here is based on a parameterization of the background values that are then subtracted from the measurements. The scheme first removes pixels with high SZA ($>70°$) and SCDs larger than 1.5 DU (measurements with presumably real SO_2) and then calculates the offset correction by averaging the SO_2 data on an ozone slant column grid. This is done independently for each across-track position and hemisphere, and the correction makes use of measurements averaged over a time period of two weeks around the measurement of interest (to improve the statistics and minimize the impact of a possible extended volcanic SO_2 plume on the averaged values). Figure S2 gives an example of the effect of the background correction and shows that the implemented correction largely solves the SO_2 SCD bias problem.

However, the correction has limitations in its parameterization. The error on the residual SCDs has been estimated by the maximum nonzero SCDs on long-term averaged global maps and is of 0.1–0.15 DU. For the two alternative fitting windows (w2 and w3), the biases are small in comparison to the column amounts expected to be retrieved in these windows (Table 1), but we have, nevertheless, implemented offset corrections using parameterizations of the background slant columns based on latitude, cross-track position, and time (2 weeks moving averages).

2.3. Air Mass Factor Calculation

The corrected slant columns are converted into SO_2 vertical column densities by applying air mass factors (AMF = SCD/VCD). The AMFs are calculated using the formulation introduced by *Palmer et al.* [2001]:

$$AMF = \int_{ground}^{TOA} WF(z) N(z) dz \tag{1}$$

where WF(z) is the so-called scattering-weighting function or box AMF, which characterizes the measurement sensitivity as a function of altitude (z), N(z) is the SO_2 a priori vertical profile shape (normalized SO_2 concentration profile), and the limits of integration are from the ground height to the top of atmosphere.

The weighting functions are determined via a multidimensional linear interpolation of WF look-up tables (three in total, one for each fitting window), generated with the LInearized Discrete Ordinate Radiative Transfer (LIDORT) version 3.3 radiative transfer model [*Spurr*, 2008]. The radiative transfer simulations assume a U.S. standard atmosphere [*Anderson et al.*, 1986] and Lambertian reflectors for the ground and the clouds. The WF look-up tables have six entries, respectively, for the solar zenith angle, viewing zenith angle, relative azimuth angle, surface albedo, effective reflector height (surface or cloud), and total ozone column. The latter is particularly important for accurate sensing of SO_2 in the boundary layer (using the baseline window) where the measurement sensitivity/optical light path is strongly dependent on the absorption of UV radiation by total atmospheric ozone. As a matter of fact, the measurement sensitivity depends on the wavelength, especially in the 312–326 nm range as a result of increased scattering and absorption (see Figure 1 and *Richter* [2009]). We have conducted sensitivity tests to determine effective wavelengths representative of the different fitting intervals. For this, we have generated synthetic spectra for typical observation conditions and SO_2 profiles using the LIDORT model, and we have done closed-loop retrievals (see Figure S3). It turns out from this exercise that calculations at 313, 326, and 375 nm give the best results, for the three fitting windows w1, w2, and w3, respectively. Note that the effective wavelength of 313 nm comes as no surprise because the SO_2 absorption (hence spectral information) is the highest at this wavelength for w1 (Figure 1).
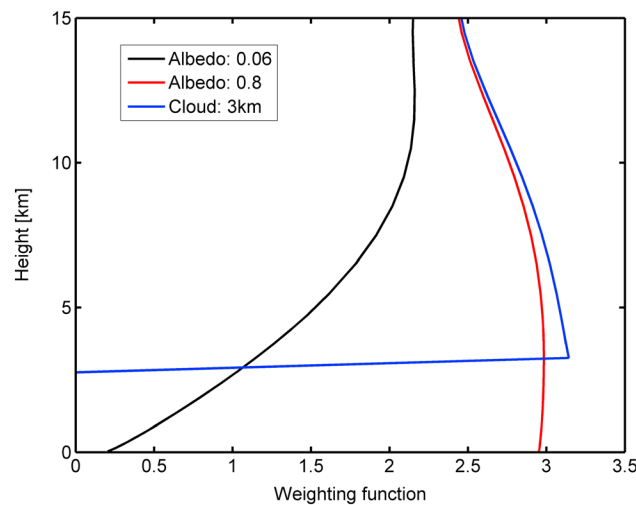
Figure 2. Scattering-weighting functions at 313 nm as function of surface albedo (0.06 and 0.8) and for a cloud top at 3 km. Calculations are made for a total ozone column of 385 DU, for a nadir-viewing geometry, and for a solar zenith angle of 40°.

The cloud is considered as a Lambertian reflecting surface, characterized by a single cloud top height and a cloud albedo of 0.8, in line with the assumption made for the OMI cloud product OMCLDO2 [*Acarreta et al.*, 2004]. For partly cloudy pixels, we use the independent pixel approximation:

$$WF(z) = \Phi WF_{cloud}(z) + (1-\Phi)WF_{clear}(z) \qquad (2)$$

where Φ is the intensity-weighted cloud radiance fraction [*Martin et al.*, 2002].

$$\Phi = \frac{f_c I_{cloud}}{f_c I_{cloud} + (1-f_c)I_{clear}} \qquad (3)$$

where f_c is the effective cloud fraction.

The WF look-up tables are used along with the corresponding intensity look-up tables.

An illustration of the weighting functions is given in Figure 2, for clear-sky cases assuming a surface albedo of 0.06 and 0.8, and for a cloudy case with a cloud top height of 3 km. The curves are for a SZA of 40°. Figure 2 shows the typical behavior of the satellite nadir UV measurement sensitivity to an absorber located at different altitudes for various surface albedo situations and for a cloudy scene. Note that the AMF formulation (equations (1) and (2)) accounts implicitly for any SO_2 column below the cloud (the so-called ghost column, not sounded by the satellite) because the integration (equation (1)) is performed down to ground height rather than cloud-top height.

In practice, the WF is evaluated for each pixel based on auxiliary data sets. The total ozone column is from a Level 2 data set of OMI [*Bhartia and Wellemeyer*, 2002; *Koukouli et al.*, 2012]. For the surface albedo, we use the climatological monthly minimum Lambertian equivalent reflect (minLER) data from *Kleipool et al.* [2008]. This database has a spatial resolution of 0.5°×0.5°. The cloud parameters (cloud fraction and cloud top height) are taken from the OMI operational OMCLDO2 product [*Acaretta et al.*, 2004].

To calculate air mass factors, weighting functions have to be convolved with realistic SO_2 vertical profile shapes (equation (1)). However, the vertical distribution of SO_2 is generally unknown, and it is sometimes even difficult to tell whether the observed SO_2 is of volcanic origin or from pollution. Therefore, the algorithm computes three vertical columns for different hypothetical SO_2 profiles including typical anthropogenic [*Krotkov et al.*, 2006] and volcanic cases. For volcanic SO_2, we consider two scenarios with 1 km box concentration profiles centered at 7 and 15 km. This approach is similar to other algorithms [*Yang et al.*, 2007; *Rix et al.*, 2012] and aims at representing volcanic plumes injected into the free troposphere and lower stratosphere, respectively. For anthropogenic SO_2, unlike in previous data, we use daily SO_2 profiles from the global tropospheric chemistry transport model Intermediate Model of the Global and Annual Evolution of Species (IMAGES), extracted at the overpass time of OMI.

The global CTM IMAGESv2 simulates the concentrations of 131 trace gases (among which 41 fast-reacting species) at a horizontal resolution of 2°×2.5° and at 40 vertical unevenly distributed levels extending from the surface to the lower stratosphere (44 hPa). Details about the current model version are given in *Stavrakou et al.* [2013]. The model time step is set to 4 h. The effects of diurnal variations in the photolysis rates, kinetic rates, meteorological fields, and the emissions are accounted for through correction factors obtained from a simulation with a 20 min time step [*Stavrakou et al.*, 2009]. These correction factors are then applied to model simulations with longer time steps.

Anthropogenic SO_2 emissions are obtained from the REASv2 inventory [*Kurokawa et al.*, 2013] over Asia, from European Monitoring and Evaluation Programme (EMEP) over Europe (http://www.ceip.at), and from the Emissions Database for Global Atmospheric Research (EDGAR3.2) FT2000 inventory for 2000 over the rest of

the world. Emissions of SO_2 from anthropogenic sources are estimated at 53.8 TgS in 2010 globally. Vegetation fires are obtained from the Global Fire Emissions Database, Version 3 database [*van der Werf et al.*, 2010] and account for 1.3 TgS in 2010. Emissions of SO_2 and other sulfur compounds from continuously degassing volcanoes are kept constant throughout the years and amount to 7.2 TgS annually [*Andres and Kasgnoc*, 1998]. Besides direct emissions, SO_2 is formed through oxidation of sulfur-containing biospheric compounds like dimethyl sulfide, carbonyl sulfide (OCS), carbon disulfide (CS_2), and hydrogen sulfide (H_2S). The global annual photochemical source is calculated at 18.1 TgS. Dry and wet deposition account for approximately 60% of the global SO_2 sink, followed by oxidation by OH (20%), and heterogeneous in-cloud reactions of SO_2 with H_2O_2 (18%) and with O_3. The aerosol simulation in IMAGESv2 is described in *Stavrakou et al.* [2013].

The AMFs calculated with the IMAGES profiles have been compared to the estimates of *Lee et al.* [2009], and we found similar results both in magnitude and for the general patterns. It should be noted that the accuracy of IMAGES-based AMFs over highly polluted regions or for point sources (see section 3.2.3 on validation) is limited due to the relatively coarse resolution of the model.

As can be seen from Figure 2, the measurement sensitivity is strongly dependent on the altitude (at least for the usual low surface reflectance case). Therefore, the algorithm stores the so-called column averaging kernel (CAK = WF/AMF) [*Eskes and Boersma*, 2003] as it enables recalculation with alternative profiles estimates or a comparison with other types of data.

3. Results

Here we present the SO_2 column results obtained with the retrieval technique described above. In section 3.1, we illustrate the algorithm for a selection of volcanic events. The results for anthropogenic SO_2 are presented in section 3.2.

3.1. Volcanic SO_2

In the following, we provide several examples of OMI SO_2 column retrievals for volcanic plumes typically injected into the UTLS. For such SO_2 plumes, the exact knowledge of their corresponding altitude is not critical, as the measurement sensitivity is only weakly dependent on the height (above ~ 10 km), even in the presence of clouds underneath the plume (Figure 2). For simplicity (and unless specified otherwise), we have used the SO_2 vertical columns assuming a box profile centered at 15 km consistent with OMI SO_2 lower stratosphere STL product. For comparison, we have also used OMI results from the PCA algorithm, assuming a similar lower stratospheric SO_2 profile centered at ~17.5 km. For the PCA retrievals, the same simplified assumptions about solar zenith angle (30°), viewing zenith angle (0°), O_3 profile (325 DU, midlatitude profile), and surface albedo (0.05) as those in the OMI standard PBL (planetary boundary layer) SO_2 product were assumed (see *Li et al.* [2013] for details). The fitting window was iteratively adjusted to longer wavelengths (from 310.5–340 nm to 320.5–340 nm) for pixels with large volcanic SO_2. A more complete PCA algorithm with more realistic assumptions for volcanic SO_2 retrievals is currently underdevelopment.

The first example is for the Kasatochi volcano (Aleutian Islands) that erupted on 7 and 8 August 2008 [*Waythomas et al.*, 2010] and emitted large quantities of SO_2 in the UTLS [*Kristiansen et al.*, 2010]. The SO_2 plume could be monitored for several weeks by many satellite instruments [e.g., *Richter et al.*, 2009; *Bobrowski et al.*, 2010; *Corradini et al.*, 2010; *Krotkov et al.*, 2010; *Clarisse et al.*, 2012; *Hörmann et al.*, 2013], as the plume dispersed throughout the Northern Hemisphere. Figure 3 compares our OMI SO_2 retrievals with the columns from the LF and PCA algorithms, for the first 2 days after the start of the eruption. The retrieved total SO_2 masses are given inset in Figure 3. For these observations, retrievals are mostly performed in w3 (typically for VCD $\gtrsim$ 100 DU) and w2 spectral windows.

For both days, the retrievals by DOAS, LF, and PCA are qualitatively consistent, with all three algorithms revealing similar spatial distribution of the volcanic SO_2 plume. For 8 August, the VCDs retrieved by DOAS and PCA are higher than the VCDs from the LF algorithm, which is to be expected because LF is known to underestimate very high SO_2 columns [*Yang et al.*, 2007; *Krotkov et al.*, 2010]. The maximum column values are 382, 354, and 222 DU for DOAS, PCA, and LF, respectively. All three retrievals show an apparent increase in the total SO_2 mass on the following day, suggesting that they probably all underestimate SO_2 for 8 August, when the volcanic plume is more concentrated with greater SO_2 loading. This is
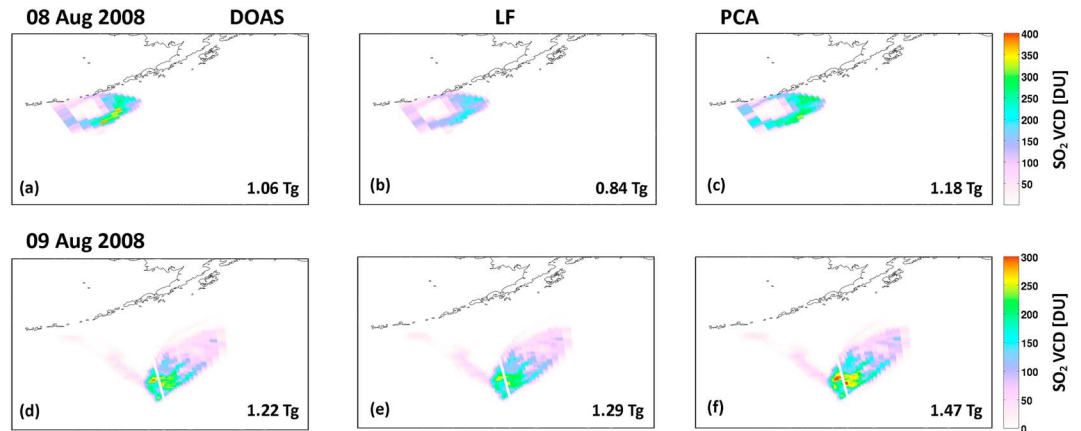
Figure 3. OMI SO_2 vertical columns for the plume of Kasatochi for 8 and 9 August 2008 (orbits 21635 and 21650), retrieved by (a, d) DOAS, (b, e) Linear Fit (STL), and (c, f) PCA algorithms. The numbers inset are the retrieved total mass of SO_2.

supported by other estimates [e.g., *Richter et al.*, 2009; *Bobrowski et al.*, 2010; *Clarisse et al.*, 2012] as well as our tests of the same DOAS algorithm on GOME-2 spectra that yielded column VCD of up to 565 DU (not shown) for the same day. Comparing these three algorithms, we also notice that the percentage increase in SO_2 mass from 8 to 9 August for LF is much greater at over 50%. This implies that LF has a greater relative negative bias for very high SO_2 columns, as also indicated by earlier studies [*Yang et al.*, 2007; *Krotkov et al.*, 2010]. Despite these differences, it is still remarkable that the three algorithms agree within 20–30% in terms of the total SO_2 mass. It should also be mentioned that some of the quantitative discrepancy could be due to different overpass times, ash loadings, viewing angles, or a combination of several effects [*Hörmann and Wagner*, 2014].

As a second case study, we illustrate our algorithm for the explosive eruption of Sarychev Peak in Russia [*Haywood et al.*, 2010] that emitted large amounts of SO_2 during the 11–19 June 2009 period. Figure 4 shows a comparison between total SO_2 mass time series measured by OMI (DOAS) and the Infrared Atmospheric Sounding Interferometer (IASI) [*Clarisse et al.*, 2012], assuming a representative plume height of 13 km. Here we have summed the contributions of all OMI pixels with columns larger than 0.27 DU (detection limit at the 3σ value level). As can be seen, the OMI results agree fairly well with the IASI data, demonstrating the ability of our algorithm to retrieve SO_2 abundances, for both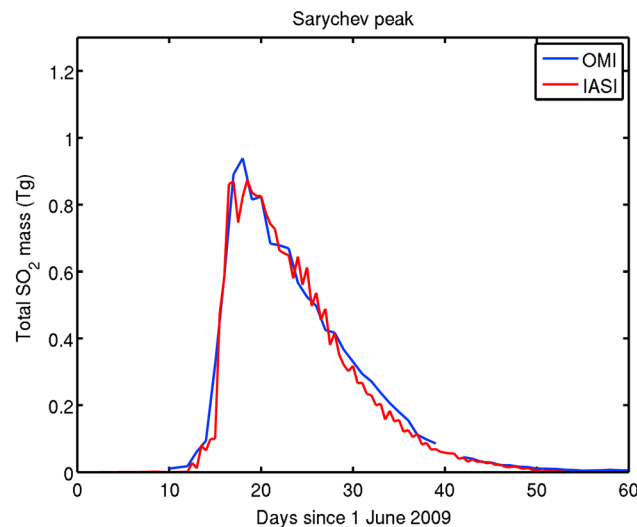 low- and high-column regimes. We have also estimated the SO_2 amount released by Sarychev during the whole eruption, using a flux determination method described by *Theys et al.* [2013]. By considering an SO_2 e-folding lifetime of 1 week (compatible with the exponential decay of the total mass in Figure 4), we found a total mass of SO_2 emitted during 11–19 June 2009 of ~1.5 Tg.

The last example is for the eruption of Grímsvötn (Iceland) on 22 and 23 May 2011, which emitted about 0.61 Tg of SO_2 at 5–13 km altitude [*Moxnes et al.*, 2014]. After several weeks, remnants of the volcanic SO_2 emissions could still be detected which allows to illustrate the performances of the algorithms for aged/filamentary plumes. Figure 5 shows a comparison of SO_2 columns over Europe between OMI DOAS, LF,
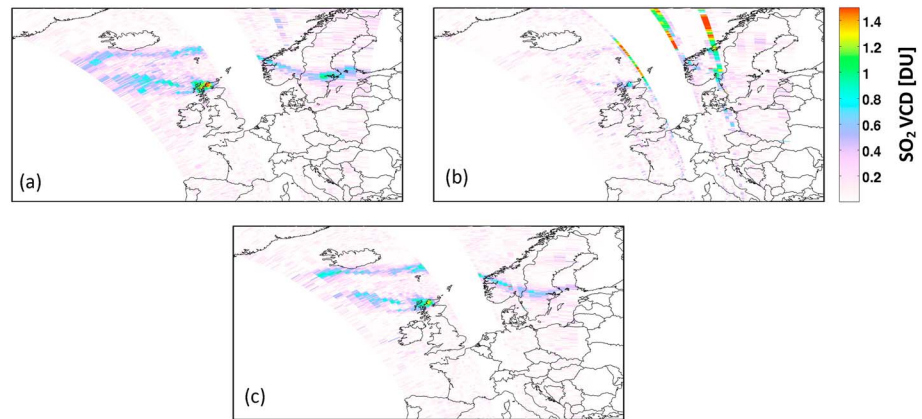

Figure 4. Total SO_2 mass measured by OMI and IASI after the eruption of Sarychev in June 2009. A plume height of 13 km is assumed.

Figure 5. OMI SO$_2$ columns over northern Europe on 13 June 2011, orbit 36759, retrieved using the (a) DOAS, (b) LF (STL) and (c) PCA algorithms.

and PCA algorithms, for measurements performed 3 weeks after the eruption of Grímsvötn. For this example, the treatment of row anomaly pixels described in section 2.2 is applied to all three algorithms.

As can be seen, the plume of SO$_2$ from Grímsvötn is clearly discernible from the background noise in the DOAS and PCA data set but is hardly detected by the LF algorithm. The reason for this feature is probably related to the failure of the empirical residual correction technique applied to the LF SO$_2$ band residuals at high latitudes [*Yang et al.*, 2007]. As this correction is based on a sliding group of pixels along the orbit track and since a significant number of those pixels are not SO$_2$ free (but are classified as such), the band residuals are likely overcorrected. Note also that the DOAS and PCA SO$_2$ columns seem to be less affected by the row anomaly issue than the LF data. This is likely because LF makes use of radiance measurements only for a few wavelengths, while DOAS and PCA exploit the full spectral information in their respective wavelength ranges. As a test, we applied the row anomaly L1B flag and found that more pixels were discarded with this standard procedure, but the artifacts visible in Figure 5b were effectively removed. Further comparisons between DOAS and PCA results are presented in section 3.2.1 for anthropogenic SO$_2$.

3.2. Anthropogenic SO$_2$

Sulfur dioxide from anthropogenic sources is largely confined in the boundary layer close to the surface. In this altitude region, the accuracy of the retrieved SO$_2$ columns is directly affected by systematic errors in the AMF input parameters, notably the SO$_2$ profile shape and surface albedo (as can be deduced from Figure 2). As a consequence, the retrieval uncertainties are large. For many emission sources, the SO$_2$ signal in the OMI spectra is smaller than the typical noise. Therefore, random sources of error are also significant and spatial-temporal averaging of SO$_2$ columns is generally needed. In the following (and unless stated otherwise), we have used AMFs calculated with the IMAGES a priori profiles, and only the pixels with effective cloud fractions, f_c, less than 0.3 have been considered. Even for these relatively clear-sky pixels, the errors on the SO$_2$ columns due to clouds can be considerable for individual scenes (especially for low clouds), due to propagation of errors in-cloud parameters and in SO$_2$ profile shape (i.e., through the ghost column correction). These effects will be quantified and discussed in more details in a separate paper.

As a first illustration, Figure 6 shows a map of OMI SO$_2$ columns averaged for multiple years (2004–2009) over Europe and western Asia. It was shown in several papers (*Carn et al.* [2007], *Fioletov et al.* [2011, 2013], *McLinden et al.* [2012], among others) that OMI is able to detect anthropogenic point sources of SO$_2$ (even small ones), and our results are in line with these studies. In Figure 6, many emission regions are depicted in great details (including several spots with very low SO$_2$ columns <0.1 DU); these are related to man-made production of SO$_2$ by coal-fired power plants, cities, oil industry (over the Persian Gulf), and smelters [e.g., *Fioletov et al.*, 2013]. The only natural volcanic source of SO$_2$ visible on the map is Mount Etna in Sicily, Italy. Over India, emissions of SO$_2$ from power plants are clearly visible and the retrieved columns are similar to the values of *Lu et al.* [2013]. Outside the geographical area of Figure 6, many other emissions hot spots are
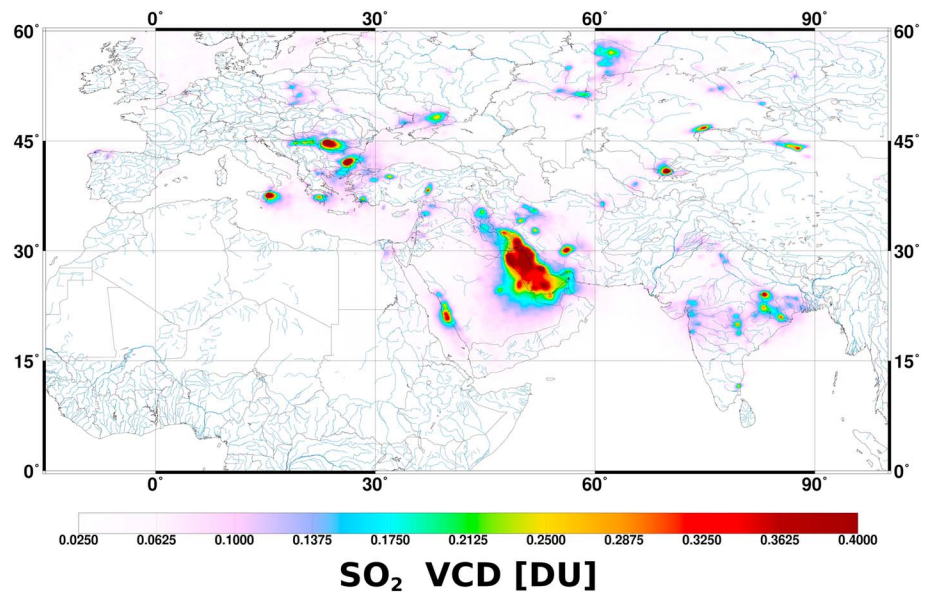
Figure 6. OMI SO_2 columns averaged for the 2004–2009 period on a 0.25° × 0.25° grid showing emission hot spots over Europe and western Asia. Cloudy pixels and measurements affected by strong volcanic eruptions are excluded from the analysis.

found and this can be appreciated on a global distribution map of SO_2 columns (Figure 7). We found evidence, in our OMI data set, for even weaker anthropogenic SO_2 signals than those presented in Figures 6 and 7, and this will be illustrated in section 3.2.4.

In the following, we have not applied any ad hoc filtering algorithm, nor had we applied local bias correction as suggested in *Fioletov et al.* [2011] and *McLinden et al.* [2012]. Applying such in the future is expected to enable detection of new point sources with even lower SO_2 signals.

In the next subsections, we evaluate the performances of our algorithm for anthropogenic SO_2 through comparisons with other satellite data sets and validation against ground-based measurements.

3.2.1. Comparison to OMI PCA Algorithm

We have compared our DOAS results with the SO_2 columns from the OMI PCA algorithm. Figure 8 shows monthly averaged SO_2 columns from DOAS and PCA, and differences between the results, for August 2006 for the eastern parts of the U.S. and China, which correspond to Figures 3 and S4 from *Li et al.* [2013]. In Figure 8, we have used the same data filtering as described by *Li et al.* [2013], as well as consistent retrieval settings for the AMF calculations. In particular, a summertime eastern U.S. SO_2 profile [*Taubman et al.*, 2006] was used for all AMF computations. Note that, over China, aircraft SO_2 profile by *Krotkov et al.* [2008] indicates a Center of Mass altitude of ~0.9 km, similar to the eastern U.S. SO_2 profiles.

Generally, the SO_2 columns with DOAS have a slightly larger noise level than PCA. Over the equatorial Pacific, we estimate a standard deviation of the DOAS SO_2 VCDs of ~0.6 DU, while the typical value for PCA is 0.5 DU (and ~1 DU for the previous OMI operational PBL product) [*Krotkov et al.*, 2008]. While the DOAS results are retrieved in the 312–326 nm window, the PCA algorithm uses the range 310.5–340 nm. We have done test retrievals by extending our fitting window toward shorter wavelengths (i.e., from 312 to 310.5 nm) and found a standard deviation of the VCDs close to 0.5 DU. Therefore, it is likely that the better performance of PCA compared to DOAS as for the noise is due to the inclusion of the strong SO_2 absorption band peaking around 310.8 nm (Figure 1) which further stabilizes the fit.

When comparing the SO_2 maps, we find that, overall, PCA and DOAS results are fairly close. Both algorithms consistently capture enhanced SO_2 signals over industrialized and densely populated areas. Over the eastern U.S. (Figures 8a and 8c), the absolute differences between DOAS and PCA columns (Figure 8e) are generally less than 0.5 DU and the DOAS algorithm has a tendency to produce more negative values than PCA. Over China, the DOAS and PCA algorithms measure similar patterns (Figures 8b and 8d), but it appears that some
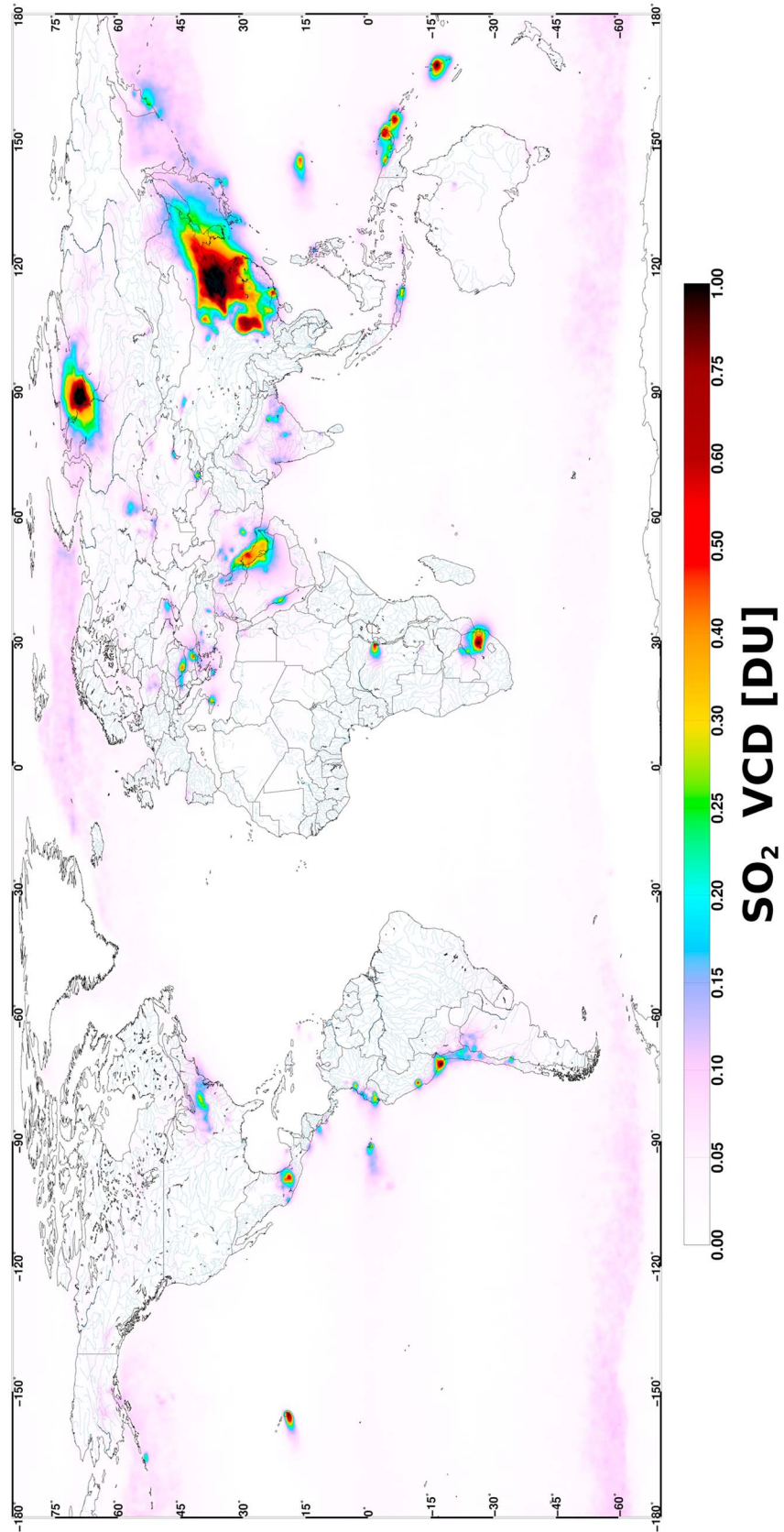
Figure 7. Global distribution of SO$_2$ columns from nearly clear-sky OMI measurements averaged for the 2004–2009 (same as Figure 6). Anthropogenic and volcanic emissions sources are visible. Note the presence of elevated SO$_2$ values over clean regions at high latitudes due to residual interferences with ozone or the Ring effect.
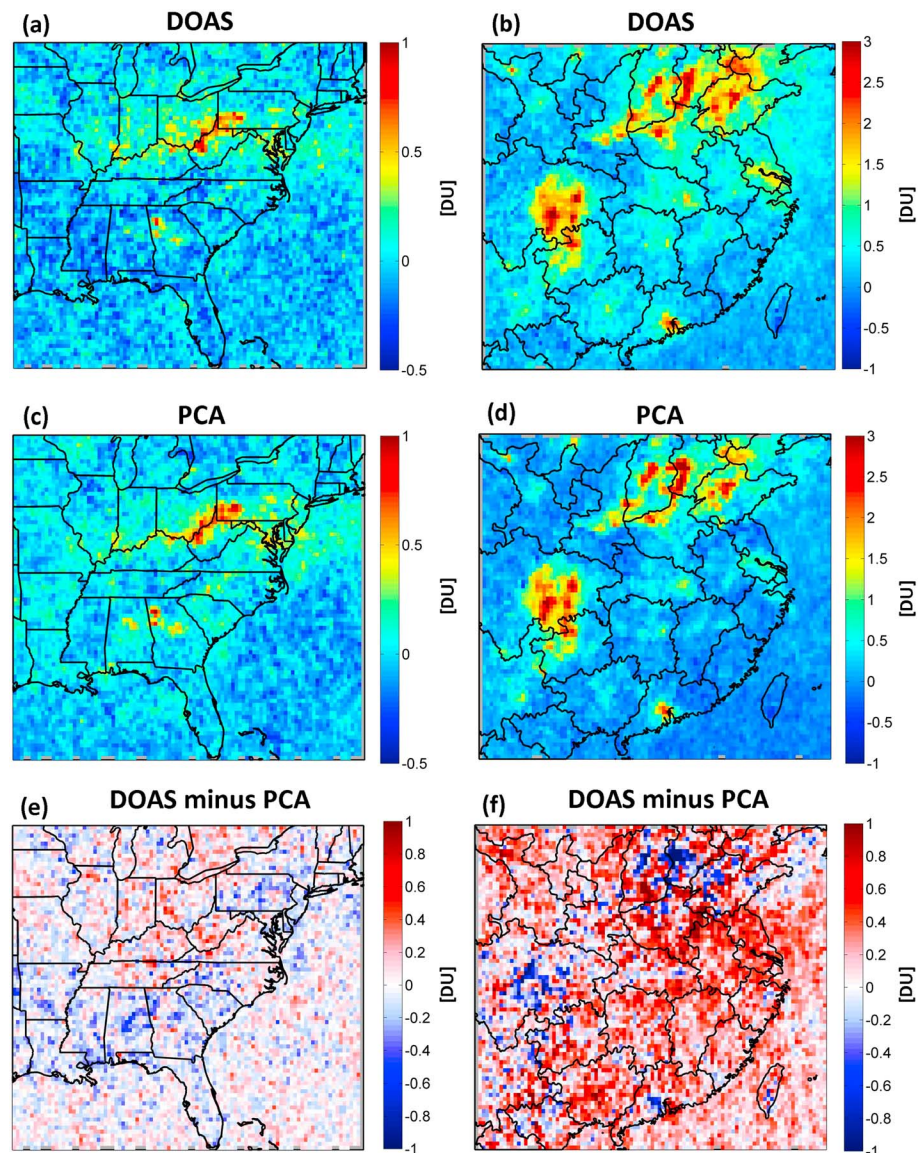
Figure 8. OMI SO_2 column maps for August 2006 over (left) eastern U.S. and (right) China retrieved using the (a, b) DOAS and (c, d) PCA algorithms for clear-sky pixels and using a fixed SO_2 profile (see text). (e, f) The SO_2 column differences between DOAS and PCA are shown in the lower maps.

SO_2 point sources are more prominent with DOAS than PCA. We also find that the DOAS retrievals have less negative values than PCA, particularly over southeastern China. Generally, the DOAS columns show larger values than PCA results, and the mean difference is +0.2 DU (Figure 8f).

The reasons for the differences between DOAS and PCA retrievals are unclear but are possibly related to (1) the selection of the wavelength range. The use of different fittings windows leads to different ozone interferences and biases in the SO_2 retrievals, (2) the absence of explicit treatment of aerosols in both DOAS and PCA algorithms, and (3) the use of a background correction scheme in the DOAS algorithm but not in the PCA scheme.

Finally, we have also compared DOAS and PCA results for other geographical regions. We clearly find better performances of the PCA algorithm for high latitudes and clean regions, although no background corrections are made in the PCA retrievals. This is probably due to the large number of principal components used that minimizes spectral misfits.
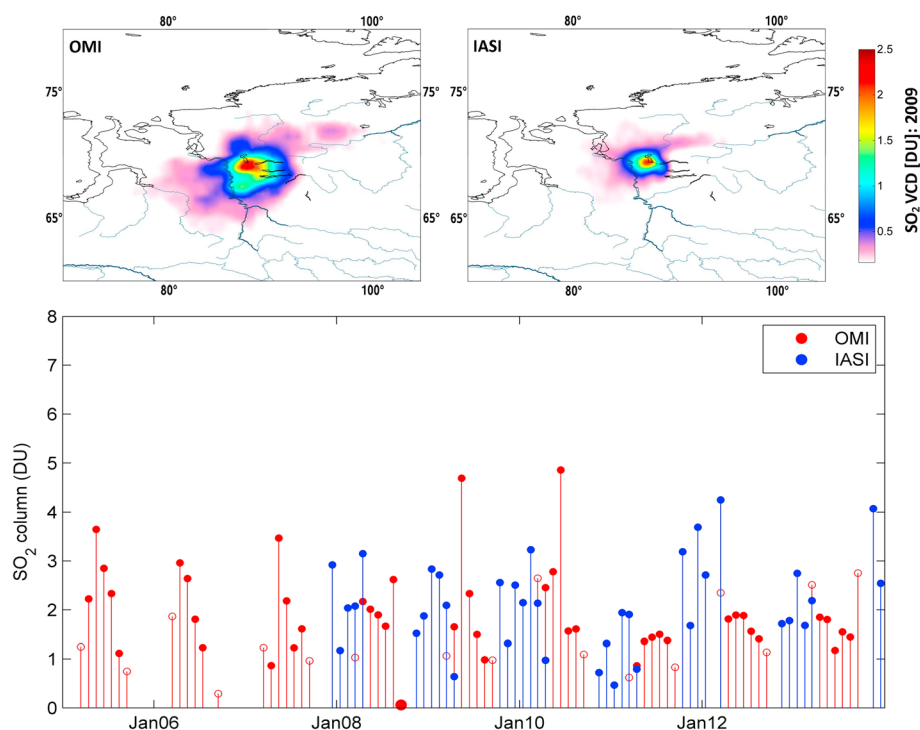
Figure 9. (top) Yearly averaged SO_2 columns measured by OMI and IASI over Norilsk for 2009. (bottom) Time series of monthly averaged SO_2 columns from OMI and IASI measurements located within 50 km around Norilsk, for 2005–2013 period. The values for months with less than 5 days of successful measurements are not displayed. The red circles correspond to OMI data with averaged solar zenith angles larger than 65°.

Further comparisons of the DOAS and PCA results are needed. It is important to understand the differences between the algorithms as it opens perspectives for improved and more robust retrievals for the small emission sources.

3.2.2. Norilsk—Comparison to IASI Data

Norilsk (69.35°N, 88.2°E) is a heavily polluted industrial city in Siberia due to intense and continuous mining and smelting of heavy metals. With an estimated flux of about 1 Mt of SO_2 per year [*Walter et al.*, 2012], the region of Norilsk produces a strong and persistent signal in the OMI SO_2 data.

Here we compare our OMI SO_2 columns with IASI retrievals. *Bauduin et al.* [2014] demonstrated the ability of a nadir thermal infrared sensor such as IASI to perform measurements of boundary layer SO_2 in the area of Norilsk. This is made possible for conditions with low humidity and large thermal contrast (TC: temperature difference between the surface and the boundary layer), typically encountered at Norilsk in winter. Figure 9 (top) shows maps of SO_2 columns averaged for 2009 by OMI (SZA $< 70°$) and IASI (0–2 km layer and $|TC| > 7$ K) over the Norilsk area. Both instruments detect similar distributions of boundary layer SO_2. However, OMI tends to measure more SO_2, the spatial pattern being more extended than with IASI. This is probably related to differences in their detection limits for near-surface SO_2. If one considers a small region around the source, OMI and IASI are then fairly close. For example, for a 50 km circle radius around Norilsk, OMI and IASI averaged SO_2 columns for 2009 are 2.1 and 2.2 DU, respectively. We note however that, strictly speaking, comparing OMI and IASI results is difficult because there are only very few measurements collocated in time; IASI retrievals are mostly successful for wintertime (polar night), while OMI is only able to measure during spring-summer at high latitudes. As an illustration, Figure 9 (bottom) also presents monthly averaged SO_2 columns time series (covering the 2005–2013 period) for OMI and IASI measurements in a 50 km radius circle centered at Norilsk. We found that the OMI and IASI values are in good agreement, and the averaged VCDs are 1.9 and 2.2 DU for OMI and IASI, respectively. The results shown in Figure 9 (bottom) also illustrate the complementarity of UV and thermal infrared soundings in their ability to monitor air pollution in Norilsk. Although it is hard to be conclusive (because measurements are usually not collocated in time), the overall time evolution of the SO_2
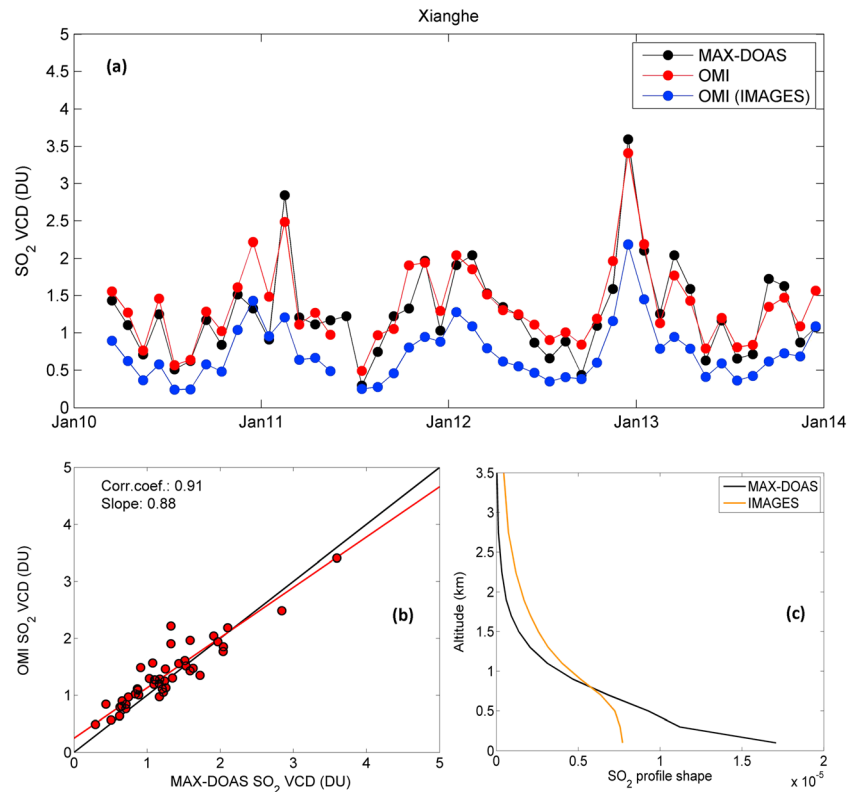
Figure 10. (a) Comparison of monthly averaged SO_2 columns at Xianghe for the period 2010–2013 measured by the MAX-DOAS and OMI (pixels falling in a 100 km radius around the station). The SO2 vertical profiles used in the OMI algorithm are either measured by the MAX-DOAS (red symbols) or modeled by IMAGES (blue symbols). No data are displayed for June 2011 because of the contamination by volcanic SO_2 from the eruption of Nabro. (b) Scatterplot of OMI SO_2 columns (calculated using the MAX-DOAS profiles) versus MAX-DOAS SO_2 columns. Statistical parameters (correlation coefficient and slope of the linear regression (red line)) are given inset. The black line is the 1:1 line. (c) Comparison between the SO_2 profile shapes (expressed in cm^{-1}) measured by the MAX-DOAS instrument and modeled by IMAGES (average values for the period March 2010 to December 2013).

columns is similarly captured by OMI and IASI. For example, we notice a decrease in SO_2 columns from the end of 2010 to mid-2011 compared to previous periods. This feature was observed by both OMI and IASI sensors.

3.2.3. Validation Over Xianghe, China

The validation of satellite measurements of anthropogenic SO_2 is a challenge for many reasons, one of which being the representativeness (or lack thereof) of the correlative data when compared to the satellite columns. Valuable studies have been undertaken to validate space-based UV SO_2 retrievals, with airborne and surface in situ measurements [e.g., *Krotkov et al.*, 2008; *Lee et al.*, 2009, 2011; *Nowlan et al.*, 2011; *He et al.*, 2012]. Nevertheless, the comparisons presented therein are either limited to short periods of time or rely on assumed vertical distribution of SO_2. Here we present a comparison of our OMI SO_2 retrievals to ground-based column and profile measurements for nearly 4 years (March 2010 to December 2013), at the suburban site of Xianghe (39.77°N, 117.0°E), China, located at about 50 km south east of Beijing.

The instrument is a multiaxis DOAS (MAX-DOAS) system developed by BIRA-IASB and operated by the Institute of Atmospheric Physics, Chinese Academy of Sciences. Owing to measurements of backscattered UV radiances performed sequentially at several elevation angles above the horizon, the lowermost troposphere is sounded with varying measurement sensitivity, and profile information on SO_2 and aerosol extinction can be retrieved from the MAX-DOAS measurements. The description of the retrieval technique and presentation of the results, including validation against in situ measurements, can be found in *Wang et al.* [2014].

The comparison between the ground-based and OMI SO_2 columns is done as follows: first, all OMI clear-sky pixels (f_c less than 0.3) within a 100 km radius circle around Xianghe, and surface height less than 500 m
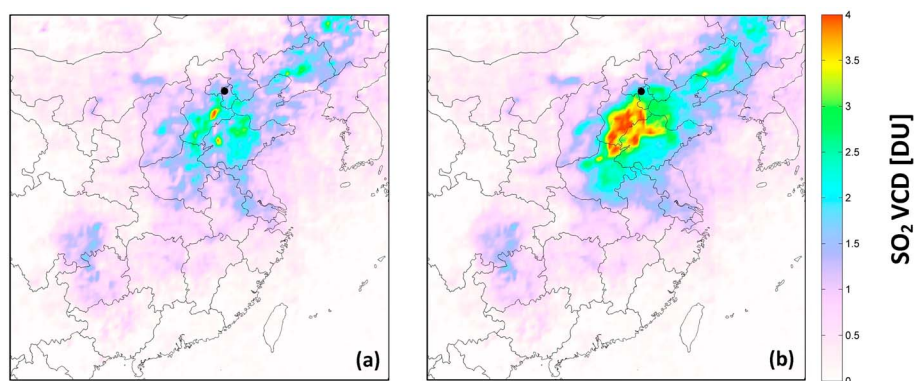
Figure 11. OMI SO_2 column maps over China for January 2013 with a selection for (a) clear-sky scenes, and (b) clear-sky and haze scenes (see text). The same AMF calculation is applied to Figures 11a and 11b. It assumes a clear-sky atmosphere and SO_2 profiles from IMAGES. A solar zenith angle cutoff of 70° is considered here. The site of Xianghe is marked by a black circle.

(to exclude observations over clean elevated regions) with solar zenith angles less than 65° are selected. Then, for each OMI pixel, all MAX-DOAS data within ± 90 min of the OMI overpass time are considered, and a mean SO_2 vertical concentration profile is estimated. To select the best profiles, we have considered only the MAX-DOAS retrievals with degrees of freedom for signal (DFS) larger than 0.7 [*Wang et al.*, 2014]. This criterion removes measurements with high aerosol loadings. Finally, the OMI SO_2 columns are corrected using new AMFs that are evaluated using WFs from OMI and the MAX-DOAS mean SO_2 profile (via equation (1)), doing so allows a consistent comparison between MAX-DOAS and OMI SO_2 VCDs.

It should be noted that the AMF calculation only uses the shape of the MAX-DOAS profile and is therefore independent of the absolute MAX-DOAS concentration values.

Figure 10a shows the comparison between the monthly averaged ground-based (black dots) and coincident OMI SO_2 columns (red dots) for the period March 2010 to December 2013 at Xianghe. One can see that the MAX-DOAS and OMI columns, corrected for the MAX-DOAS profile shape, agree very well, and the seasonal cycle of SO_2 is consistent in both data sets. We have estimated the relevant statistical parameters of the bivariate linear regression OMI versus MAX-DOAS (the scatterplot is shown in Figure 10b). The correlation coefficient is equal to 0.91, and the slope of the linear regression fit is 0.88 (but is very close to 1 if the intercept of the regression is forced to zero). These results depend of course on the accuracy of the retrieved MAX-DOAS SO_2 profile shapes used for the OMI AMFs. *Wang et al.* [2014] presented an error budget on the MAX-DOAS SO_2 retrievals, including the uncertainty related to the a priori profile. We have propagated this error through the OMI retrievals and found an uncertainty on the OMI AMFs of about 20%. This is not negligible and calls for further measurements of SO_2 in the altitude range where the MAX-DOAS has little sensitivity to SO_2.

Note that the default OMI SO_2 columns using IMAGES a priori profile shapes (displayed in Figure 10a with blue dots) tend to underestimate the MAX-DOAS column values by up to a factor of 2, because the SO_2 profile shapes from IMAGES are peaked at higher altitudes as compared with the MAX-DOAS retrievals (see Figure 10c for a comparison profile shapes). This illustrates the importance of the profiles on the retrievals.

We now proceed further and develop the validation exercise for the specific month of January 2013. During that period, an extreme pollution episode occurred over a large part of North China [e.g., *Yang et al.*, 2013; *Boynard et al.*, 2014; *Huang et al.*, 2014], and several cities were affected by a persistent haze layer. For this event, the measurement of SO_2 pollution by OMI is strongly altered by the high loadings of aerosols that absorb and scatter UV radiation and hence influence the light path through the SO_2 layer. So far, the effect of aerosols has not been considered in our AMF calculation. Another aerosol-related effect affecting the SO_2 column estimates comes from the fact that thick aerosol layers appear as reflecting surfaces (this can be observed, e.g., in true color Moderate Resolution Imaging Spectroradiometer images, http://neo.sci.gsfc.nasa.gov/) and are typically considered as clouds in the OMCLDO2 cloud product.
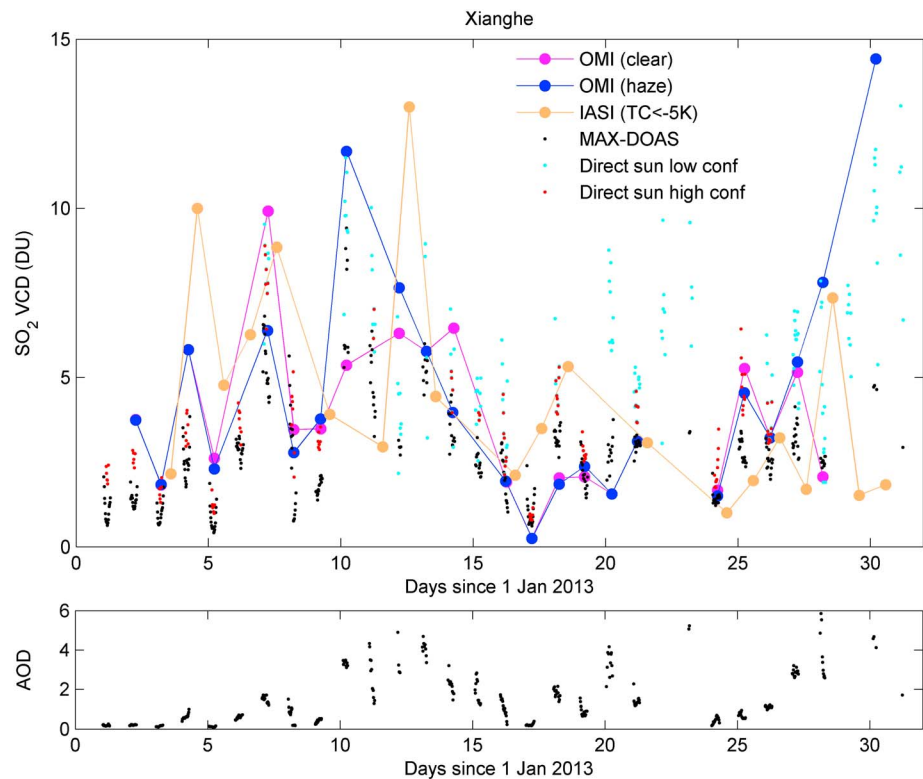
Figure 12. (top) Comparison of SO$_2$ columns from satellites (OMI and IASI daily averages) and ground-based observations for January 2013 at Xianghe. OMI results are displayed for two sets of pixels: clear-sky and haze scenes. For the latter, an aerosol correction based on the retrieved MAX-DOAS extinction profiles is applied. IASI SO$_2$ column averages have been calculated for pixels with a thermal contrast -5 K and lower and in a circle of 100 km radius around the station. The ground-based SO$_2$ columns are derived from measurements in multiaxis and direct Sun geometries (see text). (bottom) Time series of aerosol optical depth retrieved from the MAX-DOAS.

To overcome this misclassification issue, we have used a simple empirical selection of OMI pixels to pick up the scenes with thick absorbing aerosol layers close to the surface: the corresponding "haze scenes" are defined by the pixels for which the UV aerosol index is larger than 1.5 and the difference between surface pressure and OMCLDO2 retrieved effective cloud pressure is less than 150 mb. To avoid a double classification, the "clear-sky" scenes are redefined in the following as the pixels with f_c less than 0.3 and that do not fulfill the haze selection criterion. Figure 11 shows the vertical SO$_2$ column maps for January 2013 for (Figure 11a) clear-sky pixels and (Figure 11b) clear-sky and haze scenes. The vertical columns are calculated using clear-sky AMFs, and no attempt is made to correct for aerosols (the information on aerosols is not available). The aim of Figure 11 is only to illustrate the impact of the data selection. As can be seen, the SO$_2$ columns increase by up to a factor of 2 over the North China plain, when considering the haze (SO$_2$-enriched) scenes.

Although the city of Xianghe is not the region in China with highest SO$_2$ pollution (according to Figure 11), we have examined the time evolution of several SO$_2$ data sets over this site for January 2013 (Figure 12):

1. OMI clear: daily averaged SO$_2$ columns for clear-sky pixels. This data set is identical to the one in Figure 10, except that haze scenes are excluded and we have relaxed the cutoff value on the SZA to 70° to improve the statistics.

2. OMI clear and haze: same as (1) but including the haze scenes (as defined above). For the latter haze scenes, not only the SO$_2$ profiles but also the aerosol extinction profiles from the MAX-DOAS are used in the calculation of the AMFs applied to OMI. For this, we have considered a single-scattering albedo for the aerosols equal to 0.9, which is compatible with published estimates [*Zhao and Li*, 2007] and Aerosol Robotic Network measurements (http://aeronet.gsfc.nasa.gov/) at Xianghe, albeit not at UV wavelengths.

3. IASI: half-daily averaged SO_2 columns for pixels within 100 km radius around Xianghe and a thermal contrast of -5 K and lower (mostly nighttime measurements). This data set is identical to the one published in *Boynard et al.* [2014].

4. MAX-DOAS: diurnal cycles of retrieved SO_2 columns. In contrast to Figure 10, no data filtering based on DFS has been applied here, because the aim is to compare the results for various aerosol loadings (the aerosol optical depth (AOD) time series is displayed in Figure 12, bottom).

5. Direct Sun: in addition to its nominal multiaxis mode, the ground-based instrument also operates in the direct Sun geometry. For high aerosol loadings, reduced information to the whole boundary layer SO_2 may be expected for the MAX-DOAS retrievals; and therefore, the direct Sun measurements are deemed to give better results than the MAX-DOAS estimates. The direct Sun vertical columns of SO_2 are obtained by dividing absolute slant columns with air mass factors considering a geometrical light path through the SO_2 layer. The latter assumption is questionable at high AODs, and we have therefore assigned a quality flag to the direct Sun column estimates (labeled "low/high confidence" in Figure 12) as an informative piece on the validity of the geometrical approximation. This flag is evaluated empirically based on concurrent measurements of the oxygen dimer O_2-O_2, used here as a proxy of the light path in the atmosphere.

For low AODs, one can see from Figure 12 that the OMI SO_2 columns (clear) agree generally well with the MAX-DOAS estimates. For high AODs (larger than 2), the "clear" and "clear and haze" SO_2 columns are sometimes significantly different and, for these days, the clear and haze column values are commensurate with the direct Sun estimates, suggesting a sensible treatment of the aerosols for the OMI haze data set. Interestingly, most of the differences between the different OMI data arise from the pixels selection (for the haze scenes, as defined above) and not so much from the different AMFs applied. The AMFs, including the aerosols, were found to be on average only 15% (range: −20% to 40%) larger than the aerosol-free AMFs. We have inspected the MAX-DOAS SO_2 and aerosol extinction profiles for January 2013, and found that the profile shapes are quite similar. The explanation is therefore a compensation of enhancement and reduction of the SO_2 signal due to aerosols (in line with the findings of *Leitão et al.* [2010] on the impact of aerosols on satellite NO_2 retrievals). However, we note that the aerosol-corrected AMFs depend strongly on the single-scattering albedo for the aerosols, and the latter is therefore a key parameter that needs to be accurately determined for further validation work.

In Figure 12, the IASI retrievals are also displayed and compare reasonably well with the ground-based and OMI estimates, for the low column values. Conversely, there are often large differences for the SO_2 peaks. For the infrared measurements, the most important source of uncertainty is the thermal contrast (TC)—even small errors in the TC can propagate to large errors in the retrieved column. There are also several other factors that could explain the discrepancies: differences in temporal and vertical sampling of the atmosphere between UV and thermal infrared measurements, dependence of the IASI retrievals on the vertical SO_2 profile, aerosols, and clouds.

To conclude the discussion on the validation exercise at Xianghe, we note that the results of Figures 11 and 12 are not in line with the OMPS retrievals of *Yang et al.* [2013] who reported SO_2 columns over China in January 2013 a factor of 2–4 lower than our estimates.

3.2.4. Detection of Shipping Emissions

International shipping is a significant source of pollutants including CO_2, nitrogen oxides (NO_x), sulfur oxides (SO_x), volatile organic compounds, particulate matter, and black carbon. It is important to monitor those emissions as they are expected to grow in the future. Space-based observations of shipping emissions have focused on NO_2 [e.g., *Beirle et al.*, 2004; *Richter et al.*, 2004, 2011] and also formaldehyde [*Marbach et al.*, 2009], but the detection of SO_2 has hitherto not been reported in the literature. Here we evaluate our OMI SO_2 retrievals to capture the SO_2 emissions from ships.

As the IMAGES model does not include inventories of shipping emissions of SO_x, the AMFs calculated from the modeled SO_2 profiles are not appropriate for the shipping signal; and therefore, we first concentrate on retrieved slant columns instead of vertical columns. Although the noise level of the retrieved SO_2 SCDs is low (typically 0.25 DU for the standard deviation), the expected shipping signal is well below this detection limit, so we have based our analysis on long-term averages to reduce the data scatter. Five years (2005–2009) of clear-sky data (f_c less than 0.3) have been considered, and the data affected by volcanic SO_2 from strong eruptions during that period have been filtered out.
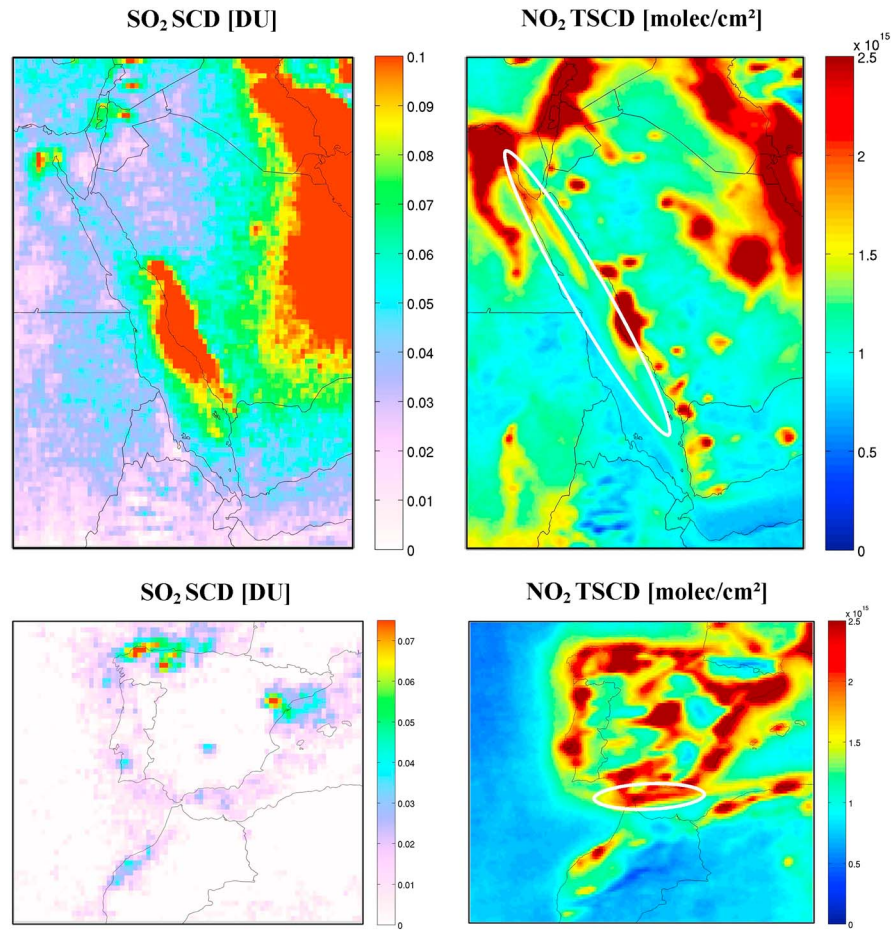
Figure 13. (left) Multiannual averaged SO$_2$ slant columns derived from clear-sky OMI measurements from 2005 to 2009 over the Middle East and Spain-North of Africa. Data strongly affected by volcanic SO$_2$ have been excluded from the analysis. (right) Tropospheric NO$_2$ slant columns are measured by OMI over the same period and regions. The shipping lanes in the Red Sea and in the vicinity of the strait of Gibraltar are shown in the NO$_2$ maps with white ellipses.
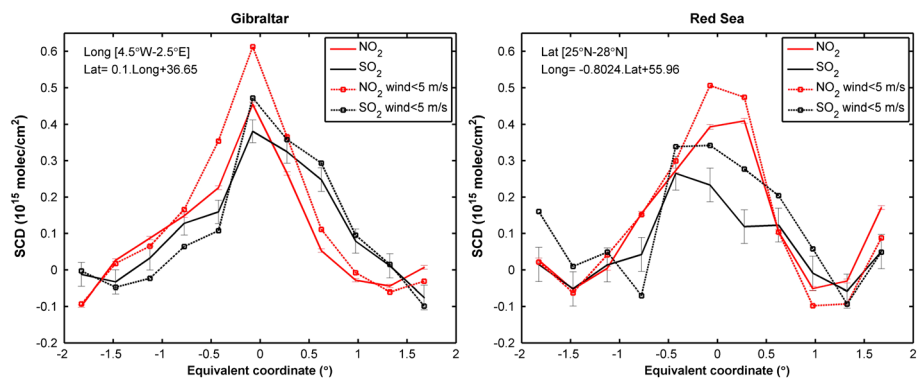

Figure 14. OMI multiannual-averaged slant columns of SO2 (black) and tropospheric NO2 (red) along ship tracks ((left) strait of Gibraltar and (right) Red Sea) presented in Figure 13. The slant columns are shown as a function of the equivalent coordinate (distance in degree from the shipping lane), and first-order polynomial fits are subtracted from the averages. (inset) The parameterizations used to locate the ship tracks are given. The selection of pixels is identical as in Figure 13, except for the dashed lines that correspond to days with low surface wind speed (less than 5 m/s). The error bars represent the errors on the mean SCDs, i.e., the standard deviation divided by the square root of the number of observations. Note that the error bars for the low wind speed values are not shown for better readability.

The SO_2 results are presented in Figure 13 for two regions, over the Middle East and Spain. Also shown are the corresponding tropospheric NO_2 slant columns measured by OMI (H. Yu et al., manuscript in preparation, 2014) to illustrate the pollution patterns in the corresponding regions. One can see enhanced SO_2 columns in the Red Sea which coincide with the shipping tracks as depicted in the NO_2 map, although the SO_2 column levels over the Red Sea cannot be attributed to ships only as there is a strong contamination by land sources (e.g., refineries near Jeddah in Saudi Arabia). As shown in Figure 13, enhanced SO_2 values are also found near the Gibraltar strait where intense shipping is notorious, as evidenced in the NO_2 data. Nevertheless, for both cases, the signal from ships appears to be close to or at the noise level. To improve the statistics, we have averaged the SO_2 and (tropospheric) NO_2 SCDs along the ship tracks to get a spatial cross section. For this, we have defined for each case (Red Sea or Gibraltar) a parameterization of the shipping lane (a simple latitude-longitude linear relationship), and we have estimated the averaged slant columns of SO_2 and NO_2 (for clear-sky pixels) as a function of the distance from the shipping lane. Compared to the gridded data (Figure 13), this reduces the noise on the SO_2 slant columns by about a factor of 5. To isolate the enhancement due to shipping emissions relative to the background, first-order polynomials were fitted and subtracted from to the SO_2 and NO_2 averages.

The SO_2 and NO_2 results are shown in Figure 14, for Gibraltar (left) and Red Sea (right) ship tracks. The error bars on the SO_2 and NO_2 values represent the error on the mean SCDs ($\sigma/\sqrt{N}$; σ is the SCD standard deviation, N is the number of observations).

For each region, one can see enhanced values of SO_2 and NO_2 well above the detection limit and centered over the middle of the ship track. We have performed these calculations also for low surface wind conditions (i.e., averaged wind speed for the lowest 0–500 m above the surface less than 5 m/s according to data from the European Centre for Medium-Range Weather Forecasts (ECMWF)), and the estimated SCDs (dashed line) increase by about 20–30% both for NO_2 and SO_2 (the corresponding error bars are not shown for better readability but are up to 70% larger than the error bars with no selection on the wind speed). This supports the shipping origin of the observed SO_2 (detection is facilitated by less plume dilution).

Shipping emissions of NO_x and SO_2 are subject to regulations by the International Maritime Organization, and the monitoring of the effective decrease in fuel sulfur content is of interest. It can be determined by the relative emission of NO_x (controlled by engine type and operation and temperature of combustion) and SO_2 through the NO_2/SO_2 ratio. We have estimated the ratio NO_2/SO_2 based on the measurements in shipping plumes in Figure 14. For this, we have applied a scaling to the NO_2/SO_2 slant column ratio to account for the difference in measurement sensitivity to NO_2 and SO_2 in the boundary layer. We obtain a typical ratio NO_2/SO_2 of 0.5–1.0, a range that is compatible, e.g., with the shipping emission estimates from aircraft measurements by *Berg et al.* [2012].

In addition to the cases shown in Figure 13, we have also looked for other examples of shipping emissions of SO_2. In the Indian Ocean, several ship tracks are clearly visible in the NO_2 data, but the detection of shipping SO_2 signal was not conclusive there. The reason for this is unclear, but we notice that the NO_2 columns (background corrected) are lower for the Indian Ocean ship tracks than in the Red Sea and near the Gibraltar strait, hence, it might be related to a detection limit issue.

As a final remark, it is worth noting the great ability of our OMI SO_2 algorithm to detect very weak emission sources also over land (sometimes with SCDs lower than 0.05 DU). In Figure 13, we can clearly identify, e.g., the Nile Valley and the coal power plants of Sines (South-West Portugal), El Jadida (Atlantic coast of Morocco), and Puertollano (South-center Spain).

4. Conclusions

We have developed an advanced algorithm to retrieve SO_2 vertical columns from UV-visible measurements and applied it to OMI data from 2004 to 2013. The retrieval scheme includes a DOAS spectral fitting, a background correction, and the calculation of air mass factors and vertical column averaging kernels. We use fixed UTLS SO_2 profiles as input to the algorithm for volcanic SO_2 plumes and simulations from the global chemical transport model IMAGES to represent SO_2 profiles for anthropogenic emissions.

Several examples of volcanic eruptions and comparisons with contemporaneous IASI, OMI Linear Fit, and OMI Principal Component Analysis retrievals demonstrate the ability of our algorithm to detect and quantify volcanic SO_2 plumes for both low and high-column regimes.

The determination of SO_2 columns for anthropogenic sources is notoriously difficult because of the low column amount and reduced measurement sensitivity close to the surface, leading to large retrieval uncertainties. Therefore, intercomparison of satellite SO_2 data and validation against ground-based measurements are especially important for anthropogenic SO_2 sources.

We have made preliminary comparisons of OMI columns retrieved from the DOAS and PCA algorithms over eastern U.S. and eastern China. The results from the two algorithms are in good overall agreement, and we found that they have very good and comparable detection limits (0.5–0.6 DU). However, more work is needed to compare the DOAS and PCA algorithms in a more systematic way to gain confidence in the detection of very weak SO_2 sources.

We have also performed comparisons between OMI columns and recently reported IASI observations of boundary layer SO_2 at Norilsk, and we found a convincing overall agreement, further illustrating the complementarity of ultraviolet and thermal infrared nadir instruments.

We have presented a validation of our OMI data with MAX-DOAS measurements in Xianghe (China) for March 2010 to December 2013. Local air mass factors have been calculated using SO_2 profile shape measurements from the ground-based instrument. We find an excellent agreement between OMI and MAX-DOAS SO_2 columns with consistent seasonal and even short-term variations. On average, the satellite and ground-based SO_2 columns agree within 12%. We have also investigated the extreme pollution case in China for January 2013 and showed that SO_2 columns from ground-based, IASI, and OMI measurements could be as high as 10–15 DU. We found that the selection of OMI pixels corresponding to haze scenes is important to reconcile the OMI and ground-based SO_2 column results. We also briefly discussed the impact of elevated aerosols on the OMI AMFs.

Finally, the ability of our algorithm to detect very weak SO_2 sources has been demonstrated on multiannual averaged SO_2 columns. Using simultaneous observations of tropospheric NO_2 and meteorological wind field data, we, for the first time, present evidence for shipping SO2 emissions with space-based observations. It is likely that such emissions will be more easily monitored with the next generation of nadir instruments, especially the TROPOMI/Sentinel-5 Precursor instrument, owing to its improved spatial resolution and signal-to-noise ratio.

References

Acarreta, J. R., J. F. de Haan, and P. Stammes (2004), Cloud pressure retrieval using the O_2-O_2 absorption band at 477 nm, *J. Geophys. Res.*, *109*, D05204, doi:10.1029/2003JD003915.

Anderson, G., S. Clough, F. Kneizys, J. Chetwynd, and E. P. Shettle (1986), AFGL atmospheric constituents profiles (0-120 km) Environmental Research Papers No. 954, ADA175173, AFGL-TR 86-0110, U.S. Air Force Geophysics Laboratory, Optical Physics Division.

Andres, R. J., and A. D. Kasgnoc (1998), A time-averaged inventory of subaerial volcanic sulfur emissions, *J. Geophys. Res.*, *103*(D19), 25,251–25,261, doi:10.1029/98JD02091.

Bauduin, S., L. Clarisse, C. Clerbaux, D. Hurtmans, and P.-F. Coheur (2014), IASI observations of sulfur dioxide (SO_2) in the boundary layer of Norilsk, *J. Geophys. Res. Atmos.*, *119*, 4253–4263, doi:10.1002/2013JD021405.

Beirle, S., U. Platt, R. von Glasow, M. Wenig, and T. Wagner (2004), Estimate of nitrogen oxide emissions from shipping by satellite remote sensing, *Geophys. Res. Lett.*, *31*, L18102, doi:10.1029/2004GL020312.

Berg, N., J. Mellqvist, J.-P. Jalkanen, and J. Balzani (2012), Ship emissions of SO_2 and NO_2: DOAS measurements from airborne platforms, *Atmos. Meas. Tech.*, *5*, 1085–1098, doi:10.5194/amt-5-1085-2012.

Bhartia, P., and C. Wellemeyer (2002), TOMS-V8 total O_3 algorithm, OMI algorithm theoretical basis document. [Available at http://www.knmi.nl/omi/documents/data/OMI_ATBD_Volume_2_V2.pdf.]

Bobrowski, N., C. Kern, U. Platt, C. Hörmann, and T. Wagner (2010), Novel SO_2 spectral evaluation scheme using the 360–390 nm wavelength range, *Atmos. Meas. Tech.*, *3*, 879–891, doi:10.5194/amt-3-879-2010.

Bogumil, K., et al. (2003), Measurements of molecular absorption spectra with the SCIAMACHY Pre-Flight Model: Instrument characterization and reference data for atmospheric remote-sensing in the 230-2380 nm region, *J. Photochem. Photobiol. A*, *157*(2-3), 167–184, doi:10.1016/S1010-6030(03)00062-5.

Boynard, A., et al. (2014), First space measurements of simultaneous pollutants in the boundary layer from IASI: A case study in the North China Plain, *Geophys. Res. Lett.*, *41*, 1–6, doi:10.1002/2013GL058333.

Brion, J., A. Chakir, J. Charbonnier, D. Daumont, C. Parisse, and J. Malicet (1998), Absorption spectra measurements for the ozone molecule in the 350-830 nm region, *J. Atmos. Chem.*, *30*, 291–299, doi:10.1023/A:1006036924364.

Carn, S. A., A. J. Krueger, N. A. Krotkov, and M. A. Gray (2004), Fire at Iraqi sulfur plant emits SO_2 clouds detected by Earth Probe TOMS, *Geophys. Res. Lett.*, *31*, L19105, doi:10.1029/2004GL020719.

Carn, S. A., A. J. Krueger, N. A. Krotkov, K. Yang, and P. F. Levelt (2007), Sulfur dioxide emissions from Peruvian copper smelters detected by the Ozone Monitoring Instrument, *Geophys. Res. Lett.*, *34*, L09801, doi:10.1029/2006GL029020.

Carn, S. A., N. A. Krotkov, K. Yang, and A. J. Krueger (2013), Measuring global volcanic degassing with the Ozone Monitoring Instrument (OMI), in *Remote Sensing of Volcanoes and Volcanic Processes: Integrating Observation and Modeling*, edited by D. M. Pyle, T. A. Mather, and J. Biggs, *Geol. Soc. London Spec. Publ.*, *380*, 229–257, doi:10.1144/SP380.12.

Chance, K., and R. J. Spurr (1997), Ring effect studies: Rayleigh scattering including molecular parameters for rotational Raman scattering, and the Fraunhofer spectrum, *Appl. Opt.*, *36*, 5224–5230, doi:10.1364/AO.36.005224.

Chin, M., and D. J. Jacob (1996), Anthropogenic and natural contributions to tropospheric sulfate: A global model analysis, *J. Geophys. Res.*, *101*(D13), 18,691–18,699, doi:10.1029/96JD01222.

Clarisse, L., D. Hurtmans, C. Clerbaux, J. Hadji-Lazaro, Y. Ngadi, and P.-F. Coheur (2012), Retrieval of sulphur dioxide from the infrared atmospheric sounding interferometer (IASI), *Atmos. Meas. Tech.*, *5*, 581–594, doi:10.5194/amt-5-581-2012.

Corradini, S., L. Merucci, A. J. Prata, and A. Piscini (2010), Volcanic ash and SO_2 in the 2008 Kasatochi eruption: Retrievals comparison from different IR satellite sensors, *J. Geophys. Res.*, *115*, D00L21, doi:10.1029/2009JD013634.

Danckaert, T., C. Fayt, M. Van Roozendael, I. De Smedt, V. Letocart, A. Merlaud, and G. Pinardi (2012), Qdoas Software User Manual, Version 2.1. [Available at http://uv-vis.aeronomie.be/software/QDOAS/QDOAS_manual_2.1_201212.pdf.]

Dobber, M., et al. (2006), Ozone monitoring instrument calibration, *IEEE Trans. Geosci. Remote Sens.*, *44*(5), 1209–1238, doi:10.1109/TGRS.2006.869987.

Eisinger, M., and J. P. Burrows (1998), Tropospheric sulfur dioxide observed by the ERS-2 GOME instrument, *Geophys. Res. Lett.*, *25*(22), 4177–4180, doi:10.1029/1998GL900128.

Eskes, H. J., and K. F. Boersma (2003), Averaging kernels for DOAS total column satellite retrievals, *Atmos. Chem. Phys.*, *3*, 1285–1291, doi:10.5194/acp-3-1285-2003.

Fayt, C., and M. Van Roozendael (2001), WinDOAS 2.1, Software User Manual, Belgian Institute for Space Aeronomy, Brussels, Belgium. [Available at http://bro.aeronomie.be/WinDOAS-SUM-210b.pdf.]

Fioletov, V. E., C. A. McLinden, N. Krotkov, M. D. Moran, and K. Yang (2011), Estimation of SO_2 emissions using OMI retrievals, *Geophys. Res. Lett.*, *38*, L21811, doi:10.1029/2011GL049402.

Fioletov, V. E., et al. (2013), Application of OMI, SCIAMACHY, and GOME-2 satellite SO_2 retrievals for detection of large emission sources, *J. Geophys. Res. Atmos.*, *118*, 11,399–11,418, doi:10.1002/jgrd.50826.

Greenblatt, G. D., J. J. Orlando, J. B. Burkholder, and A. R. Ravishankara (1990), Absorption measurements of oxygen between 330 and 1140 nm, *J. Geophys. Res.*, *95*(D11), 18,577–18,582, doi:10.1029/JD095iD11p18577.

Haywood, J. M., et al. (2010), Observations of the eruption of the Sarychev volcano and simulations using the HadGEM2 climate model, *J. Geophys. Res.*, *115*, D21212, doi:10.1029/2010JD014447.

He, H., et al. (2012), SO_2 over central China: Measurements, numerical simulations and the tropospheric sulfur budget, *J. Geophys. Res.*, *117*, D00K37, doi:10.1029/2011JD016473.

Hermans, C., A. C. Vandaele, and S. Fally (2009), Fourier transform measurements of SO_2 absorption cross sections: I. Temperature dependence in the 24 000–29 000 cm^{-1} (345–420 nm) region, *J. Quant. Spectrosc. Radiat. Transfer*, *110*, 756–765, doi:10.1016/j.jqsrt.2009.10.031.

Hörmann, C., and T. Wagner (2014), Radiative transfer effects of high SO_2 and aerosol loads during major volcanic eruptions, presentation given at OMI Sc, Team Meeting, Utrecht, March 2014. [Available at http://www.knmi.nl/omi/research/project/meetings/ostm18/pres_ostm18_2014.php.]

Hörmann, C., H. Sihler, N. Bobrowski, S. Beirle, M. Penning de Vries, U. Platt, and T. Wagner (2013), Systematic investigation of bromine monoxide in volcanic plumes from space by using the GOME-2 instrument, *Atmos. Chem. Phys.*, *13*, 4749–4781, doi:10.5194/acp-13-4749-2013.

Huang, K., G. Zhuang, Q. Wang, J. S. Fu, Y. Lin, T. Liu, L. Han, and C. Deng (2014), Extreme haze pollution in Beijing during January 2013: Chemical characteristics, formation mechanism and role of fog processing, *Atmos. Chem. Phys. Discuss.*, *14*, 7517–7556, doi:10.5194/acpd-14-7517-2014.

Intergovernmental Panel on Climate Change (2013), *Climate Change 2013: The Physical Science Basis. Contribution of Working Group I to the Fifth Assessment Report of the Intergovernmental Panel on Climate Change*, edited by T. F. Stocker et al., 1535 pp., Cambridge Univ. Press, Cambridge, U. K., and New York.

Khokhar, M. F., C. Frankenberg, M. Van Roozendael, S. Beirle, S. Kühl, A. Richter, U. Platt, and T. Wagner (2005), Satellite observations of atmospheric SO_2 from volcanic eruptions during the time period of 1996 to 2002, *J. Adv. Space Res.*, *36*(5), 879–887, doi:10.1016/j.asr.2005.04.114.

Kleipool, Q. L., M. R. Dobber, J. F. de Haan, and P. F. Levelt (2008), Earth surface reflectance climatology from 3 years of OMI data, *J. Geophys. Res.*, *113*, D18308, doi:10.1029/2008JD010290.

Koukouli, M., D. Balis, D. Loyola, P. Valks, W. Zimmer, N. Hao, J.-C. Lambert, M. Van Roozendael, C. Lerot, and R. Spurr (2012), Geophysical validation and long-term consistency between GOME-2/MetOp-A total ozone column and measurements from the sensors GOME/ERS-2, SCIAMACHY/ENVISAT and OMI/Aura, *Atmos. Meas. Tech.*, *5*, 2169–2181, doi:10.5194/amt-5-2169-2012.

Kristiansen, N. I., et al. (2010), Remote sensing and inverse transport modeling of the Kasatochi eruption sulfur dioxide cloud, *J. Geophys. Res.*, *115*, D00L16, doi:10.1029/2009JD013286.

Krotkov, N. A., S. A. Carn, A. J. Krueger, P. K. Bhartia, and K. Yang (2006), Band residual difference algorithm for retrieval of SO_2 from the Aura Ozone Monitoring Instrument (OMI), *IEEE Trans. Geosci. Remote Sens.*, *44*(5), 1259–1266, doi:10.1109/TGRS.2005.861932.

Krotkov, N. A., et al. (2008), Validation of SO_2 retrievals from the Ozone Monitoring Instrument over NE China, *J. Geophys. Res.*, *113*, D16S40, doi:10.1029/2007JD008818.

Krotkov, N. A., M. R. Schoeberl, G. A. Morris, S. Carn, and K. Yang (2010), Dispersion and lifetime of the SO_2 cloud from the August 2008 Kasatochi eruption, *J. Geophys. Res.*, *115*, D00L20, doi:10.1029/2010JD013984.

Krueger, A. J., L. S. Walter, P. K. Bhartia, C. C. Schnetzler, N. A. Krotkov, I. Sprod, and G. J. S. Bluth (1995), Volcanic sulfur dioxide measurements from the total ozone mapping spectrometer instruments, *J. Geophys. Res.*, *100*(D7), 14,057–14,076, doi:10.1029/95JD01222.

Kurokawa, J., T. Ohara, T. Morikawa, S. Hanayama, G. Janssens-Maenhout, T. Fukui, K. Kawashima, and H. Akimoto (2013), Emissions of air pollutants and greenhouse gases over Asian regions during 2000–2008: Regional Emission inventory in ASia (REAS) version 2, *Atmos. Chem. Phys.*, *13*, 11,019–11,058, doi:10.5194/acp-13-11019-2013.

Lee, C., R. V. Martin, A. van Donkelaar, G. O'Byrne, N. Krotkov, A. Richter, L. G. Huey, and J. S. Holloway (2009), Retrieval of vertical columns of sulfur dioxide from SCIAMACHY and OMI: Air mass factor algorithm development, validation, and error analysis, *J. Geophys. Res.*, *114*, D22303, doi:10.1029/2009JD012123.

Lee, C., R. V. Martin, A. van Donkelaar, H. Lee, R. R. Dickerson, J. C. Hains, N. Krotkov, A. Richter, K. Vinnikov, and J. J. Schwab (2011), SO_2 emissions and lifetimes: Estimates from inverse modeling using in situ and global, space-based (SCIAMACHY and OMI) observations, *J. Geophys. Res.*, *116*, D06304, doi:10.1029/2010JD014758.

Leitão, J., A. Richter, M. Vrekoussis, A. Kokhanovsky, Q. J. Zhang, M. Beekmann, and J. P. Burrows (2010), On the improvement of NO_2 satellite retrievals—Aerosol impact on the airmass factors, *Atmos. Meas. Tech.*, *3*, 475–493, doi:10.5194/amt-3-475-2010.

Levelt, P. F., G. H. J. van den Oord, M. R. Dobber, A. Mälkki, H. Visser, J. de Vries, P. Stammes, J. Lundell, and H. Saari (2006), The ozone monitoring instrument, *IEEE Trans. Geo. Rem. Sens.*, *44*(5), 1093–1101, doi:10.1109/TGRS.2006.872333.

Li, C., Q. Zhang, N. Krotkov, D. Streets, K. He, S.-C. Tsay, and J. F. Gleason (2010), Recent large reduction in sulfur dioxide from Chinese power plants observed by the ozone monitoring instrument, *Geophys. Res. Lett.*, *37*, L08807, doi:10.1029/2010GL042594.

Li, C., J. Joiner, N. A. Krotkov, and P. K. Bhartia (2013), A fast and sensitive new satellite SO2 retrieval algorithm based on principal component analysis: Application to the ozone monitoring instrument, *Geophys. Res. Lett.*, *40*, 6314–6318, doi:10.1002/2013GL058134.

Lu, Z., D. G. Streets, B. de Foy, and N. A. Krotkov (2013), Ozone monitoring instrument observations of interannual increases in SO_2 emissions from Indian coal-fired power plants during 2005-2012, *Environ. Sci. Technol.*, *13*(24), 13,993–14,000, doi:10.1021/es4039648.

Marbach, T., S. Beirle, U. Platt, P. Hoor, F. Wittrock, A. Richter, M. Vrekoussis, M. Grzegorski, J. P. Burrows, and T. Wagner (2009), Satellite measurements of formaldehyde from shipping emissions, *Atmos. Chem. Phys.*, *9*, 8223–8234, doi:10.5194/acp-9-8223-2009.

Martin, R. V., et al. (2002), An improved retrieval of tropospheric nitrogen dioxide from GOME, *J. Geophys. Res.*, *107*(D20), 4437, doi:10.1029/2001JD001027.

McLinden, C. A., V. Fioletov, K. F. Boersma, N. Krotkov, C. E. Sioris, J. P. Veefkind, and K. Yang (2012), Air quality over the Canadian oil sands: A first assessment using satellite observations, *Geophys. Res. Lett.*, *39*, L04804, doi:10.1029/2011GL050273.

Moxnes, E. D., N. I. Kristiansen, A. Stohl, L. Clarisse, A. Durant, K. Weber, and A. Vogel (2014), Separation of ash and sulfur dioxide during the 2011 Grímsvötn eruption, *J. Geophys. Res. Atmos.*, *119*, 7477–7501, doi:10.1002/2013JD021129.

Nowlan, C. R., X. Liu, K. Chance, Z. Cai, T. P. Kurosu, C. Lee, and R. V. Martin (2011), Retrievals of sulfur dioxide from the Global Ozone Monitoring Experiment 2 (GOME-2) using an optimal estimation approach: Algorithm and initial validation, *J. Geophys. Res.*, *116*, D18301, doi:10.1029/2011JD015808.

Palmer, P. I., D. J. Jacob, K. Chance, R. V. Martin, R. J. D. Spurr, T. P. Kurosu, I. Bey, R. Yantosca, A. Fiore, and Q. Li (2001), Air mass factor formulation for spectroscopic measurements from satellites: Application to formaldehyde retrievals from the Global Ozone Monitoring Experiment, *J. Geophys. Res.*, *106*(D13), 14,539–14,550, doi:10.1029/2000JD900772.

Platt, U., and J. Stutz (2008), *Differential Optical Absorption Spectroscopy (DOAS), Principle and Applications*, Springer, Heidelberg, Germany.

Puķīte, J., S. Kühl, T. Deutschmann, U. Platt, and T. Wagner (2010), Extending differential optical absorption spectroscopy for limb measurements in the UV, *Atmos. Meas. Tech.*, *3*, 631–653, doi:10.5194/amt-3-631-2010.

Richter, A. (2009), Algorithm theoretical basis document for the GOME-2 rapid volcanic SO_2 product, SAVAA project. [Available at http://savaa.nilu.no/PublicArchive.aspx.]

Richter, A., V. Eyring, J. P. Burrows, H. Bovensmann, A. Lauer, B. Sierk, and P. J. Crutzen (2004), Satellite measurements of NO_2 from international shipping emissions, *Geophys. Res. Lett.*, *31*, L23110, doi:10.1029/2004GL020822.

Richter, A., F. Wittrock, and J. P. Burrows (2006), SO_2 measurements with SCIAMACHY, in *Proceeding of Atmospheric Science Conference, Frascati, Italy, 8–12 May*, *ESA Publ. SP-628*, ESA/ESRIN, Noordwijk, Netherlands.

Richter, A., F. Wittrock, A. Schönhardt, and J. P. Burrows (2009), Quantifying volcanic SO_2 emissions using GOME-2 measurements Geophys. Res. Abstr., EGU2009-7679, EGU General Assembly 2009, Vienna, Austria.

Richter, A., M. Begoin, A. Hilboll, and J. P. Burrows (2011), An improved NO_2 retrieval for the GOME-2 satellite instrument, *Atmos. Meas. Tech.*, *4*, 1147–1159, doi:10.5194/amt-4-1147-2011.

Rix, M., et al. (2012), Volcanic SO_2, BrO and plume height estimations using GOME-2 satellite measurements during the eruption of Eyjafjallajökull in May 2010, *J. Geophys. Res.*, *117*, D00U19, doi:10.1029/2011JD016718.

Robock, A. (2000), Volcanic eruptions and climate, *Rev. Geophys.*, *38*(2), 191–219, doi:10.1029/1998RG000054.

Spurr, R. (2008), LIDORT and VLIDORT: Linearized pseudo-spherical scalar and vector discrete ordinate radiative transfer models for use in remote sensing retrieval problems, in *Light Scattering Reviews*, vol. 3, edited by A. Kokhanovsky, Springer, Chichester, U. K.

Stavrakou, T., J.-F. Müller, I. De Smedt, M. van Roozendael, G. van der Werf, L. Giglio, and A. Guenther (2009), Evaluating the performance of pyrogenic and biogenic emission inventories against one decade of space-based formaldehyde columns, *Atmos. Chem. Phys.*, *9*, 1037–1060, doi:10.5194/acp-9-1037-2009.

Stavrakou, T., J.-F. Müller, K. F. Boersma, R. J. van der A, J. Kurokawa, T. Ohara, and Q. Zhang (2013), Key chemical NO_x sink uncertainties and how they influence top-down emissions of nitrogen oxides, *Atmos. Chem. Phys.*, *13*, 9057–9082, doi:10.5194/acp-13-9057-2013.

Taubman, B. F., J. C. Hains, A. M. Thompson, L. T. Marufu, B. G. Doddridge, J. W. Stehr, C. A. Piety, and R. R. Dickerson (2006), Aircraft vertical profiles of trace gas and aerosol pollution over the mid- Atlantic United States: Statistics and meteorological cluster analysis, *J. Geophys. Res.*, *111*, D10S07, doi:10.1029/2005JD006196.

Theys, N., et al. (2013), Volcanic SO_2 fluxes derived from satellite data: A survey using OMI, GOME-2, IASI and MODIS, *Atmos. Chem. Phys.*, *13*, 5945–5968, doi:10.5194/acp-13-5945-2013.

Vandaele, A.-C., C. Hermans, P. C. Simon, M. Carleer, R. Colin, S. Fally, M. F. Mérienne, A. Jenouvrier, and B. Coquart (1998), Measurements of the NO_2 absorption cross-section from 42000 cm^{-1} to 10000 cm^{-1} (238–1000 nm) at 220 K and 294 K, *J. Quant. Spectrosc. Radiat. Transfer*, *59*, 171–184, doi:10.1016/S0022-4073(97)00168-4.

van der Werf, G. R., J. T. Randerson, L. Giglio, G. J. Collatz, M. Mu, P. S. Kasibhatla, D. C. Morton, R. S. DeFries, Y. Jin, and T. T. van Leeuwen (2010), Global fire emissions and the contribution of deforestation, savanna, forest, agricultural, and peat fires (1997–2009), *Atmos. Chem. Phys.*, *10*, 11,707–11,735, doi:10.5194/acp-10-11707-2010.

Veefkind, P., et al. (2012), TROPOMI on the ESA Sentinel-5 Precursor: A GMES mission for global observations of the atmospheric composition for climate, air quality and ozone layer applications, *Remote Sens. Environ.*, *120*, 70–83, doi:10.1016/j.rse.2011.09.027.

Vountas, M., V. V. Rozanov, and J. P. Burrows (1998), Ring effect: Impact of rotational Raman scattering on radiative transfer in Earth's atmosphere, *J. Quant. Spectrosc. Radiat. Transfer*, *60*(6), 943–961, doi:10.1016/S0022-4073(97)00186-6.

Walter, D., K.-P. Heue, A. Rauthe-Schöch, C. A. M. Brenninkmeijer, L. N. Lamsal, N. A. Krotkov, and U. Platt (2012), Flux calculation using CARIBIC DOAS aircraft measurements: SO_2 emission of Norilsk, *J. Geophys. Res.*, *117*, D11305, doi:10.1029/2011JD017335.

Wang, T., et al. (2014), Evaluation of tropospheric SO_2 retrieved from MAX-DOAS measurements in Xianghe, China, *Atmos. Chem. Phys.*, *14*, 11,149–11,164, doi:10.5194/acp-14-11149-2014.

Waythomas, C. F., W. E. Scott, S. G. Prejean, D. J. Schneider, P. Izbekov, and C. J. Nye (2010), The 7–8 August 2008 eruption of Kasatochi Volcano, central Aleutian Islands, Alaska, *J. Geophys. Res.*, *115*, B00B06, doi:10.1029/2010JB007437.

Yang, K., N. A. Krotkov, A. J. Krueger, S. A. Carn, P. K. Bhartia, and P. F. Levelt (2007), Retrieval of large volcanic SO_2 columns from the Aura Ozone Monitoring Instrument: Comparison and limitations, *J. Geophys. Res.*, *112*, D24S43, doi:10.1029/2007JD008825.

Yang, K., R. R. Dickerson, S. A. Carn, C. Ge, and J. Wang (2013), First observations of SO2 from the satellite Suomi NPP OMPS: Widespread air pollution events over China, *Geophys. Res. Lett.*, *40*, 4957–4962, doi:10.1002/grl.50952.

Zhao, F., and Z. Li (2007), Estimation of aerosol single scattering albedo from solar direct spectral radiance and total broadband irradiances measured in China, *J. Geophys. Res.*, *112*, D22S03, doi:10.1029/2006JD007384.